



On mantle chemical and thermal heterogeneities and anisotropy as mapped by inversion of global surface wave data

A. Khan,^{1,2} L. Boschi,³ and J. A. D. Connolly⁴

Received 19 February 2009; revised 2 June 2009; accepted 29 June 2009; published 18 September 2009.

[1] We invert global observations of fundamental and higher-order Love and Rayleigh surface wave dispersion data jointly at selected locations for 1-D radial profiles of Earth's mantle composition, thermal state, and anisotropic structure using a stochastic sampling algorithm. Considering mantle compositions as equilibrium assemblages of basalt and harzburgite, we employ a self-consistent thermodynamic method to compute their phase equilibria and bulk physical properties (P , S wave velocity and density). Combining these with locally varying anisotropy profiles, we determine anisotropic P and S wave velocities to calculate dispersion curves for comparison with observations. Models fitting data within uncertainties provide us with a range of profiles of composition, temperature, and anisotropy. This methodology presents an important complement to conventional seismic tomography methods. Our results indicate radial and lateral gradients in basalt fraction, with basalt depletion in the upper and enrichment of the upper part of the lower mantle, in agreement with results from geodynamical calculations, melting processes at mid-ocean ridges, and subduction of chemically stratified lithosphere. Compared with preliminary reference Earth model (PREM) and seismic tomography models, our velocity models are generally faster in the upper transition zone (TZ) and slower in the lower TZ, implying a steeper velocity gradient. While less dense than PREM, density gradients in the TZ are also steeper. Mantle geotherms are generally adiabatic in the TZ, whereas in the upper part of the lower mantle, stronger lateral variations are observed. The retrieved anisotropy structure agrees with previous studies indicating positive as well as laterally varying upper mantle anisotropy, while there is little evidence for anisotropy in and below the TZ.

Citation: Khan, A., L. Boschi, and J. A. D. Connolly (2009), On mantle chemical and thermal heterogeneities and anisotropy as mapped by inversion of global surface wave data, *J. Geophys. Res.*, 114, B09305, doi:10.1029/2009JB006399.

1. Introduction

[2] The oceanic crust is continuously being formed at mid-ocean ridge spreading centers through the active differentiation and melting of mantle peridotites. This process generates a basaltic oceanic crust that overlies the residual depleted complement, harzburgite [Ringwood, 1975]. The lithosphere thus formed is physically and chemically stratified as the topmost dominantly basaltic layer (6–10 km thick) is mineralogically different from the underlying harzburgitic and peridotitic lithospheric layers [Hofmann, 1997]. At subduction zones, meanwhile, cold oceanic lithosphere is continuously being cycled back into the

mantle because of its excess density, and, given the evidence suggested by global seismic tomography images of slab penetration, is able to reach the bottom of the mantle [Van der Hilst *et al.*, 1991; Grand, 1994; Bijwaard *et al.*, 1998]. As the slab descends into the mantle subducted material is being deposited at various depths as it becomes neutrally buoyant. The material so accumulated at the different levels is subsequently dispersed throughout the mantle by the background mantle flow [Christensen and Hofmann, 1994; Xie and Tackley, 2004; Davies, 2006; Nakagawa *et al.*, 2009]. As time proceeds thermal equilibration acts to reduce rheological and density differences ensuring that the dispersed material mixes more effectively into the surrounding mantle. Although seismology indicates that the long-wavelength component of Earth's mantle heterogeneity is generally dominant [e.g., Becker and Boschi, 2002], the above processes are responsible for producing mantle heterogeneities at all scales, radial as lateral, for which ample seismological and chemical evidence has accumulated [e.g., Hofmann, 1997; Helffrich and Wood, 2001; Tackley *et al.*, 2005].

[3] The mantle heterogeneities produced through the subduction process are thus present at all levels and

¹Niels Bohr Institute, University of Copenhagen, Copenhagen, Denmark.

²On leave at Institute of Geophysics, Swiss Federal Institute of Technology, Zurich, Switzerland.

³Institute of Geophysics, Swiss Federal Institute of Technology, Zurich, Switzerland.

⁴Institute for Mineralogy and Petrology, Swiss Federal Institute of Technology, Zurich, Switzerland.

throughout the upper and lower mantle and comprise several scale lengths from ~ 1000 km (cold subducted lithosphere, transition zone topography) to ~ 10 km (patches of lithospheric slabs that scatter seismic waves in the lower mantle) [Helffrich, 2002, 2006] and down to microscopic (chemistry) [Hofmann, 1997], and represent the various stages in the mixing process.

[4] In spite of this first-order model for the production and maintenance of lateral heterogeneities in the mantle, and in the upper in particular, we still lack a clear understanding of the nature of these heterogeneities at the various length scales observed, i.e., are they of compositional or thermal origin, or even a combination thereof, and what is the relation of these, if any, to the mode of mantle convection? Moreover, is the concept of distinct end-member compositions, suggested by the asthenospheric melting scenario, appropriate for describing mantle chemistry at large scales?

[5] One key to addressing these questions is found, in part, in the images obtained from seismic tomography, which have provided indispensable information on the large-scale structure of Earth's interior [e.g., Grand *et al.*, 1997; Masters *et al.*, 2000; Boschi and Ekström, 2002; Gung *et al.*, 2003; Debayle *et al.*, 2005; Panning and Romanowicz, 2006; Nettles and Dziewonski, 2008; Kustowski *et al.*, 2008]. In turn, physical structure offers clues about the thermal state and chemical composition of the mantle. Unfortunately, the separation of thermal and chemical effects from seismic wave velocities alone is difficult and complicated further by the relative insensitivity of seismic velocities to the density contrasts that drive mantle convection. Thus, additional information, such as that provided by seismic anisotropy, is important for the deconvolution of these effects, and seismic tomography has also been used to map anisotropy in the mantle.

[6] Seismic anisotropy is generally believed to derive from mantle minerals having a lattice preferred orientation [e.g., Tanimoto and Anderson, 1984; Karato, 1998; Montagner, 1998], produced by deformation processes needed to align individual crystals, and manifests itself through polarization anisotropy where a horizontally polarized wave, for example, travels at a different speed than a wave of vertical polarization. As anisotropy thus likely reflects present-day mantle strain field or past deformations frozen in the lithosphere, it provides a tool by which mantle flow can be mapped.

[7] Radial or transverse anisotropy was first introduced in order to explain the apparent incompatibility between Love and Rayleigh wave dispersion characteristics [e.g., Anderson, 1961; McEvilly, 1964; Forsyth, 1975; Montagner and Kennett, 1996]. The preliminary reference Earth model (PREM) model [Dziewonski and Anderson, 1981] extended this to global scale by incorporating a radially anisotropic layer in the upper 220 km of the mantle. Extension of this to more regionalized studies found significant lateral variations in anisotropy to exist beneath continents and oceans [e.g., Nishimura and Forsyth, 1989; Maupin and Cara, 1992; Leveque *et al.*, 1998; Ekström and Dziewonski, 1998; Debayle and Kennett, 2000; Silveira and Stutzmann, 2002; Sebai *et al.*, 2006; Lebedev *et al.*, 2006].

[8] Global 3-D anisotropic models have existed for some years now and are based on a variety of data. The resolution of upper mantle radial and azimuthal anisotropy involved

fundamental mode surface waves [e.g., Nataf *et al.*, 1986; Ekström and Dziewonski, 1998; Boschi and Ekström, 2002; Shapiro and Ritzwoller, 2002; Beghein and Trampert, 2004; Zhou *et al.*, 2006], overtones [Ritsema *et al.*, 2004; Gung *et al.*, 2003; Debayle *et al.*, 2005; Beghein *et al.*, 2006; Maggi *et al.*, 2006; Beucler and Montagner, 2006; Visser *et al.*, 2008a], body waves [Boschi and Dziewonski, 2000] and combinations of body and surface waves to map anisotropy throughout the mantle [Panning and Romanowicz, 2006; Kustowski *et al.*, 2008]. These studies found important 3-D variations in upper mantle anisotropy that locally differs from the PREM average. Although anisotropic variations in the middle and lower mantle were observed, these were generally found to be inconsistent among the different models, suggesting that anisotropy in these regions is not well resolved.

[9] With this in mind and in view of the limitations that seismic tomography studies suffer, including adherence to spherically symmetric seismic reference models, limited data sensitivity with respect to all physical properties, and not least the inherent shortcoming of first obtaining profiles of seismic velocities from observations and then interpreting these in terms of mantle composition and temperature, it is the purpose here to invert geophysical data directly for mantle composition, thermal state and anisotropy structure. The method that we use is based on a self-consistent thermodynamic calculation of mineral phase equilibria and their physical properties, allowing the prediction of radial profiles of seismic P and S wave velocities and density that depend only on composition, temperature and pressure (depth) [Connolly, 2005]. This results in more physically realistic models, with a natural scaling between P and S wave velocities on the one hand and density on the other, obviating recourse to less well founded and ad hoc scaling relationships usually invoked in 3-D seismic tomography studies [e.g., Panning and Romanowicz, 2006; Visser *et al.*, 2008a; Kustowski *et al.*, 2008]. Moreover, in our approach size and location of discontinuities in physical properties associated with pressure induced mineralogical phase changes, are modeled in a physically realistic manner, as their variations depend on composition and physical conditions of the particular model being considered, unlike what is usually done in seismic tomography studies where the discontinuities tend to be parameterized according to PREM.

[10] Attempts to map out the extent of radial as well as lateral variations in mantle chemistry and temperature have to some extent been undertaken before [e.g., Shapiro and Ritzwoller, 2004; Trampert *et al.*, 2004; Cammarano and Romanowicz, 2007; Ritsema *et al.*, 2009]. However, these studies typically solve a much simplified problem, by either considering an ad hoc parameterization consisting of only a subset of parameters or simply fixing composition and then inverting for potential temperature.

[11] The data that we consider here are the phase velocity maps of Visser *et al.* [2008a] and include Love and Rayleigh wave phase velocities from fundamental and up to fifth and sixth mode (overtone), respectively, and were obtained by Visser *et al.* [2008a] after a first linear inversion of their global phase delay database. The higher modes have sensitivity in the transition zone and upper part of the lower mantle. Laterally, we are restricted to the resolution of

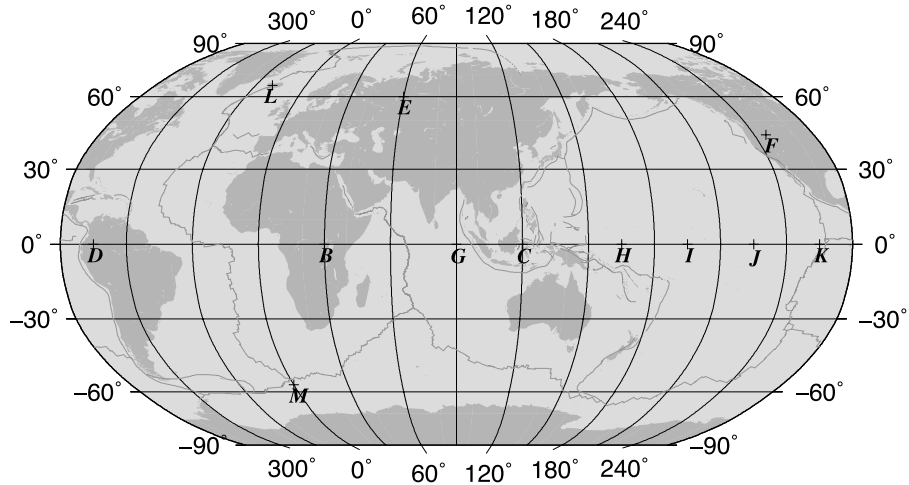


Figure 1. Global map of the Earth showing the location of the 12 sites investigated here. Note that A does not appear as it is reserved for prior information.

Visser et al. [2008a], whose maps are defined on a $5^\circ \times 5^\circ$ grid. We presently follow the idea of *Shapiro and Ritzwoller* [2004], and simultaneously invert local Love and Rayleigh wave dispersion curves extracted from the global phase velocity maps of *Visser et al.* [2008a] for a number of locations on the Earth.

[12] To invert the dispersion curves at each location, we employ a stochastic sampling algorithm, based on a Markov chain Monte Carlo (MCMC) method to propose 1-D radial models of composition, temperature and anisotropy. For every model proposed we calculate geophysical data and compare these to observations. Models that fit data within uncertainties are retained whereas models that do not are discarded. Details of the method can be found in our previous work [e.g., *Khan et al.*, 2006, 2007, 2008]. Although computationally much more involved, stochastic sampling algorithms such as MCMC methods are better suited to deal with strongly nonlinear inverse problems as is the case here. However, determining the global 3-D mantle structure via a fully nonlinear Monte Carlo inversion is computationally very expensive, and will be left as future work.

2. Surface Wave Dispersion Data

[13] The sensitivity of Love and Rayleigh wave phase velocities to the physical structure of crust and mantle varies with frequency, with longer period waves sensing deeper. This means that Love and Rayleigh wave phase velocities have resolving power in the radial direction. In addition, surface waves provide good constraints on the lateral heterogeneity of the mantle given (1) a reasonable raypath coverage and (2) that the sensitivity of surface waves to mantle structure is to a good approximation constant along a raypath. The data set that we analyze consists of the global azimuthal anisotropic phase velocity maps of fundamental and higher mode Love (up to fifth order) and Rayleigh (up to sixth order) waves of *Visser et al.* [2008a] and represents the isotropic part (azimuthally averaged) of these phase velocity maps. At a number of geographical locations distributed across the globe (see Figure 1) we extracted from the phase velocity maps Love and Rayleigh wave

dispersion curves for the fundamental and higher modes. At each location then, we have 13 dispersion curves consisting of a total of 149 distinct Love and Rayleigh wave phase velocities as a function of frequency. These 13 dispersion curves form a local data set, that we invert jointly for local compositional, thermal and radial anisotropy structure.

3. Forward Problem

3.1. Constructing the Forward Problem

[14] We consider a spherical Earth, which varies laterally and radially in properties. At each geographical point of interest, we represent our local model of the Earth by a number of layers of varying thickness, corresponding to crust, upper and lower mantle layers (details are given in section 4.2). The crust is represented by a local physical model, whereas upper and lower mantle layers are delineated by model parameters related to composition, temperature and anisotropy. It is implicitly assumed that all parameters mentioned depend on geographical position and depth.

[15] Calculating data from a set of model parameters using physical law(s) can be written in short-hand notation as $\mathbf{d} = \mathbf{g}(\mathbf{m})$, where \mathbf{m} are the above mentioned model parameters, \mathbf{d} data, i.e., Love and Rayleigh wave phase velocities ($C_R(\omega)$ and $C_L(\omega)$) as a function of frequency and geographical position, and \mathbf{g} comprises the physical law(s).

[16] The complete forward problem to be solved here can be decomposed as

$$\{c, T\} \xrightarrow{\mathbf{g}_1} \{M\} \xrightarrow{\mathbf{g}_2} \{V_p, V_s, \rho\} \xrightarrow{\mathbf{g}_3} \{V_{pv}, V_{ph}, V_{sv}, V_{sh}\} \xrightarrow{\mathbf{g}_4} \{C_R, C_L\}$$

$\{\xi, \phi, \eta\}$
 $\downarrow \mathbf{g}_3$

where c and T are compositional and thermal variables, respectively, M denotes mineral phase proportions (modal mineralogy), V_p, V_s, ρ, S wave velocity and density, ξ, ϕ, η anisotropy parameters (defined in section 3.3), and $V_{sv}, V_{sh}, V_{pv}, V_{ph}$ are velocities of vertically (v) and horizontally (h) polarized S waves and vertically and horizontally propagating P waves, respectively. \mathbf{g}_1 is the Gibbs free

Table 1. Model End-Member Bulk Compositions^a

Component	Basalt	Harzburgite
CaO	13.05	0.5
FeO	7.68	7.83
MgO	10.49	46.36
Al ₂ O ₃	16.08	0.65
SiO ₂	50.39	43.64
Na ₂ O	1.87	0.01

^aIn wt %.

energy minimization routine, which calculates modal mineralogy; g_2 estimates bulk isotropic physical properties; g_3 determines anisotropic properties; g_4 computes Love and Rayleigh wave dispersion curves.

[17] To determine the mineralogical structure and corresponding mass density, it is also necessary to specify the pressure profile. For this purpose the pressure is obtained by integrating the load from the surface (boundary condition $p = 10^5$ Pa). In sections 3.2 and 3.3 the different g are described in somewhat more detail, while parameters are delineated in section 3.5.

3.2. Petrological Model and Gibbs Free Energy Minimization

[18] We characterize mantle composition by a single depth-dependent variable that represents the weight fraction of basalt in a basalt-harzburgite mixture. For a given basalt fraction, composition is computed from

$$\mathbf{X}(z) = [1 - y(z)]\mathbf{X}_H + y(z)\mathbf{X}_B \quad (1)$$

where $\mathbf{X}(z)$ is the composition within the system Na₂O-CaO-FeO-MgO-Al₂O₃-SiO₂ (NaCFMAS) at depth z , $y(z)$ describes the relative proportions by weight of basalt and harzburgite, and \mathbf{X}_H and \mathbf{X}_B are NaCFMAS basalt and harzburgite end-member model compositions, respectively (see Table 1). The latter compositions are chosen such that the composition for $y = 0.2034$ corresponds, within uncertainties, to the pyrolite composition of *Lyubetskaya and Korenaga* [2007]. Although this compositional model has fewer degrees of freedom than those employed in our previous work, we adopt it here because it is less ambiguously related to dynamical processes.

[19] *Xu et al.* [2008] consider two types of basalt-harzburgite mantle composition models that they refer to as mechanical mixture and equilibrium models. The mechanical mixture model represents the extreme scenario in which pyrolitic mantle has undergone complete differentiation to basaltic and harzburgitic rocks. In this model bulk properties are computed by averaging the properties of the minerals in the basaltic and harzburgitic end-members. In the equilibrium model, it is assumed that harzburgitic and basaltic components are chemically equilibrated and bulk properties are computed from the mineralogy obtained by free energy minimization for the resulting bulk composition. Assuming a pyrolitic bulk mantle composition, *Xu et al.* [2008] find, on the basis of a qualitative comparison, that the mechanical mixture model provides a better match in the transition zone to seismological models such as PREM and AK135 [*Kennett et al.*, 1995] than does the equilibrium assemblage. However, from a petrological perspective a

fully segregated model for the Earth's mantle is undesirable because it is inconsistent with basaltic volcanism at mid-ocean ridges. For this reason, we employ the equilibrium model here. The mineralogy for this model is computed as a function of pressure, temperature and composition by free energy minimization using the thermodynamic data compiled by *Xu et al.* [2008]. The elastic moduli and densities for the individual minerals obtained by the free energy minimization procedure are combined by Voigt-Reuss-Hill averaging to estimate the corresponding bulk properties [*Connolly and Kerrick*, 2002; *Connolly*, 2005].

[20] Components not considered include TiO₂, Cr₂O₃ and H₂O, as well as partial melt because of a lack thermodynamic data. With regard to the less abundant elements, these are most likely to affect locations of phase boundaries, rather than physical properties, as discussed by *Stixrude and Lithgow-Bertelloni* [2005].

[21] Like *Xu et al.* [2008] we assume perfectly elastic limiting behavior, disregarding attenuation that causes dispersion of seismic waves and lower seismic velocities [*Anderson and Given*, 1982]. Our reasons for not including anelastic effects are (1) the large uncertainty and limited spatial resolution of seismologically determined attenuation models [*Romanowicz and Mitchell*, 2007], (2) the paucity of empirical data on attenuation at mantle conditions [e.g., *Stixrude and Jeanloz*, 2007], and (3) uncertainty as to whether the existing empirical data obtained at ~MHz frequencies can be reliably extrapolated to seismic frequencies as questioned by *Deschamps and Trampert* [2004] and *Stacey and Davis* [2004]. Also, the global phase velocity maps of *Visser et al.* [2008a] from which our data derive have not been corrected for attenuation-related dispersion.

3.3. Anisotropy

[22] A recurring assumption in surface wave tomography studies is that of material symmetry to reduce the number of unknowns needed to describe the anisotropic model. An anisotropic elastic medium in the general case is defined by 21 independent elements of the fourth-order elastic tensor, whereas an isotropic solid is described by only two. In the case of transverse anisotropy (symmetry axis in vertical direction), the number of independent unknowns reduces to 5, which, depending on the particular parameterization, could be V_{sv} , V_{sh} , V_{pv} , V_{ph} and η , where the former are as defined before, and η provides a rule of how the velocity evolves as the incidence angle varies between horizontal and vertical.

[23] Love in his original formulation employed the 5 coefficients A , C , F , L and N to describe an anisotropic medium of hexagonal symmetry, with axis of symmetry in the vertical direction [*Love*, 1927]. These Love coefficients are given in terms of seismic velocities by the following relations:

$$A = \rho V_{ph}^2, C = \rho V_{pv}^2, L = \rho V_{sv}^2, N = \rho V_{sh}^2, F = \frac{\eta}{A - 2L}.$$

We can now work with either set of parameters, i.e., $\{A, C, L, N, F\}$ or $\{V_{ph}, V_{pv}, V_{sh}, V_{sv}, \eta\}$. However, as the phase equilibrium calculation (section 3.2) outputs isotropic P and S wave velocities, we instead follow *Panning and Romanowicz* [2006] and *Babuska and Cara* [1991] and

reparameterize the above coefficients using the Voigt average of the isotropic P and S wave velocities

$$V_s^2 = \frac{2V_{sv}^2 + V_{sh}^2}{3} \quad (2)$$

$$V_p^2 = \frac{V_{pv}^2 + 4V_{ph}^2}{5} \quad (3)$$

in addition to the following three anisotropy parameters

$$\xi = \frac{V_{sh}^2}{V_{sv}^2}, \phi = \frac{V_{pv}^2}{V_{ph}^2}, \eta = \frac{F}{A - 2L}, \quad (4)$$

where ξ and ϕ are seen to be measures of S and P wave anisotropy, respectively. In the general case isotropic P and S wave velocities depend on all four seismic velocities as well as η or equivalently on all five Love coefficients [Babuska and Cara, 1991]. However, assuming anisotropy to be small, i.e., $\eta \sim 1$, enables us to separate the equations so that V_s only depends on V_{sv} and V_{sh} and equivalently for V_p . From a knowledge of $\{V_p, V_s, \xi, \phi, \eta\}$ then, it is straightforward to determine anisotropic velocities using equations (2)–(4), which are then subsequently employed to determine Love and Rayleigh wave dispersion curves at the different locations of interest.

[24] We would like to note that while our formulation of anisotropy is decoupled from our thermodynamic calculation of isotropic material properties, this reflects a present-day lack of knowledge of anisotropic properties for relevant minerals, rather than theoretical understanding. The theoretical formulation belying the thermodynamic approach is indeed capable of considering anisotropy [e.g., Stixrude and Lithgow-Bertelloni, 2005].

4. Inverse Problem

4.1. Formulation and Solution of the Inverse Problem

[25] In an inverse problem the relationship between model \mathbf{m} and data \mathbf{d} is usually written as

$$\mathbf{d} = \mathbf{g}(\mathbf{m}) \quad (5)$$

where \mathbf{g} in the general case is a nonlinear operator. Central to the formulation of the Bayesian approach to inverse problems is the extensive use of probability density functions (pdf's) to delineate various sources of information specific to the problem [Tarantola and Valette, 1982]. These include probabilistic prior information on model and data parameters, $f(\mathbf{m})$ (for the present brief discussion we limit ourselves to a functional dependence on \mathbf{m} and omit any reference to \mathbf{d}), and the physical laws that relate data to the unknown model parameters. Using Bayes theorem, these pdf's are combined to yield the posterior *pdf* in the model space

$$\sigma(\mathbf{m}) = kf(\mathbf{m})\mathcal{L}(\mathbf{m}) \quad (6)$$

where k is a normalization constant and $\mathcal{L}(\mathbf{m})$ is the likelihood function, which in probabilistic terms, can be

interpreted as a measure of misfit between the observations and the predictions from model \mathbf{m} .

[26] We follow the approach of our previous studies (the reader is referred to Khan *et al.* [2007] for details), and employ a Metropolis algorithm (a Markov chain Monte Carlo method) to sample the posterior distribution in the model space. Because of the generally complex shape of the posterior distribution in the model space, typically employed measures such as means and covariances are generally inadequate descriptors. Instead we present the solution in terms of a large collection of models sampled from the posterior probability density. While this algorithm is based on a random sampling of the model space, only models that result in a good data fit and are consistent with prior information are frequently sampled. We next describe parameterization and prior information (section 4.2), and the likelihood function (section 4.3).

4.2. Prior Information

4.2.1. Crust

[27] As surface waves are sensitive to crustal structure, we chose to employ as an initial starting model CRUST2.0, which is a global model that specifies crustal structure (ρ , V_p , V_s , and Moho depth) on a $2^\circ \times 2^\circ$ grid (<http://mahi.ucsd.edu/Gabi/rem.html>). At each particular geographic location, we extract the local crustal structure from CRUST2.0. We model the crust as consisting of four layers with the first four depth nodes fixed, while the fifth (the Moho) is variable. In each layer ρ , V_p and V_s are variable and perturb these parameters from the local model extracted from CRUST2.0 within certain bounds that satisfy $p_1 \leq p_2 \leq p_3 \leq p_4 \leq p_5$, where p is either ρ , V_p or V_s , and subscripts 1 to 4 refer to the 4 crustal layers. Thus, in the crust, ρ , V_p or V_s are assumed to be non-decreasing as a function of depth. Lower bounds on p_1 are $\rho = 1.5 \text{ g/cm}^3$, $V_p = 2.5 \text{ km/s}$ and $V_s = 1.5 \text{ km/s}$, while p_5 is the corresponding thermodynamically determined parameter at the first node in the mantle. Moho depth d_{cr} is left variable to within $\pm 5 \text{ km}$ of the crustal thickness specified by CRUST2.0 (13 parameters).

4.2.2. Temperature

[28] The temperature T in a given layer k is determined from $T_k = T_{k-1} + \alpha \cdot (T_{k+1} - T_{k-1})$, where α is a uniformly distributed random number in the interval $[0; 1]$. No lower or upper bounds are applied, except for surface temperature, which is held constant at 0°C . Temperatures are evaluated at 26 depth nodes at intervals of 50 km in the depth range 0–700 km, and 100 km in the range from 700 to 2886 km (26 parameters).

4.2.3. Layer Thickness

[29] The radius of the Earth and its outer core are fixed at 6371 km and 3480 km, respectively, the latter in accordance with PREM. We model upper, middle, and lower mantle as consisting of four layers with variable composition and thickness. Depths to layer boundaries (d_1, \dots, d_4) are assumed uniformly distributed in the following intervals (starting from the surface) $d_1 \in [200; 450 \text{ km}]$, $d_2 \in [450; 750 \text{ km}]$, $d_3 \in [800; 1500 \text{ km}]$, while d_4 is fixed at the core mantle boundary (3 parameters).

4.2.4. Mantle Composition

[30] We work with basalt fraction as our main compositional variable, which is assumed to vary linearly with depth

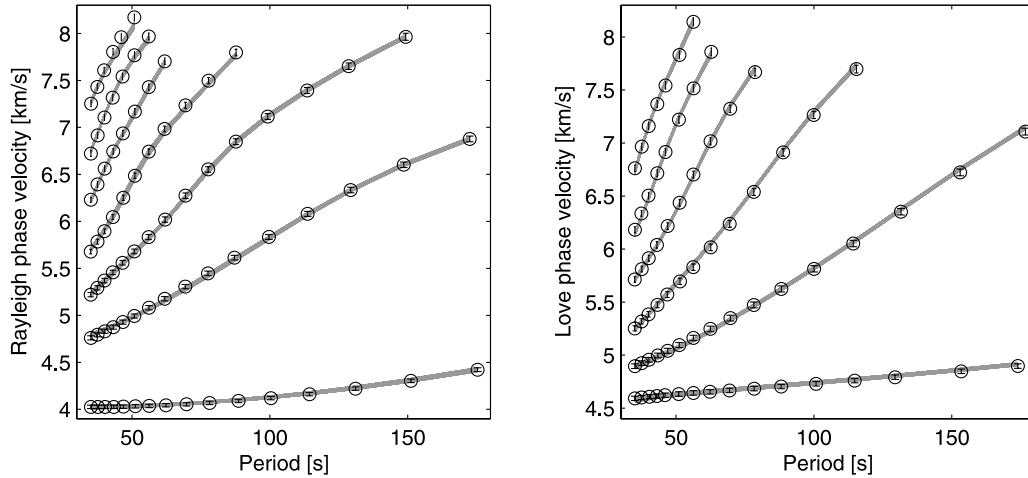


Figure 2. Comparison of calculated (gray lines) and observed data (Rayleigh and Love wave phase velocities as a function of frequency) including uncertainties (circles and error bars) for the location in the Indian Ocean at 90°E and 0°N .

within each of the aforementioned layers. The composition as a function of depth is determined from equation (1), while at each of the 5 depth nodes that delineate the 4 mantle layers, basalt fraction is assumed uniformly distributed between upper and lower limits. At the first node, bounds are $[0.15; 0.3]$, while for the remaining nodes we have $[0; 1]$. In addition, composition is assumed continuous across layer boundaries (5 parameters).

4.2.5. Anisotropy

[31] We consider anisotropic functionals of the form

$$\xi(z) = 1 + \exp\left[\frac{-z_i\Delta}{z_m}\right] \sin\left[\frac{z_i\zeta_s}{z_m}\right] \quad (7)$$

$$\phi(z) = 1 + \exp\left[\frac{-z_i\Delta}{z_m}\right] \sin\left[\frac{z_i\zeta_p}{z_m}\right] \quad (8)$$

$$\eta(z) = 1 - \exp\left[\frac{-z_i\Delta}{z_m}\right] \sin\left[\frac{z_i\zeta_\eta}{z_m}\right] \quad (9)$$

where Δ , ζ_s , ζ_p and ζ_η are model parameters, respectively, that determine the specific form of the functionals, z_i are fixed depth nodes at which anisotropy is evaluated (see section 4.2.6), and z_m is the depth to which data provide information (here $z_m = 1200$ km) and below which all anisotropy parameters equal 1, i.e., no anisotropy. The parameters are assumed to be log-uniformly distributed with no upper bound. The particular functional form for ξ , ϕ and η was chosen so as to minimize number of parameters, while at the same time emulating anisotropic functionals typically employed elsewhere, including sign changes and diminution of signal amplitude as a function of depth (for further discussion, see section 5.5, where a priori information on ξ is specifically shown). Since the crust is not expected to be anisotropic, ξ , ϕ and η are also required to be 1 in the crust and at the Moho. This requirement might have a smoothing effect on our solutions for anisotropy in the uppermost upper mantle, but will not limit resolution in the rest of the upper mantle, transition zone and upper part of the lower mantle (4 parameters).

4.2.6. Parameterization

[32] In summary, the present problem is delineated by 50 parameters in all that need to be determined at each location. This parameterization reflects the knowledge obtained from a number of trial inversions to establish a “working” model, i.e., a model whose parameterization has been optimized in the sense of producing the best misfit with the least amount of parameters. Given values of the 50 unknown model parameters, the thermodynamic model is used to establish mineralogy, density and physical properties within the silicate layers at 93 depth nodes (at intervals of 10 km in the depth range 0–710 km and 100 km in the depth range from 800 to 2600 km) from the surface downward as a function of pressure, temperature and composition.

4.3. Sampling the Posterior

[33] We assume that data noise can be modeled using a gaussian distribution and that observational uncertainties and calculation errors between Rayleigh and Love waves are independent. On the basis of this, the likelihood function is given by

$$\mathcal{L}(\mathbf{m}) \propto \exp\left(-\sum_{\text{mode}} \sum_{\text{frequency}} \frac{[d_{obs}^R - d_{cal}^R(\mathbf{m})]^2}{2\sigma_R^2} - \sum_{\text{mode}} \sum_{\text{frequency}} \frac{[d_{obs}^L - d_{cal}^L(\mathbf{m})]^2}{2\sigma_L^2}\right)$$

where d_{obs} denotes observed data, $d_{cal}(\mathbf{m})$ calculated data, superscripts R and L , Rayleigh and Love waves, respectively, and $\sigma_{R,L}$ uncertainty on either of these.

[34] In every iteration one of the following sets of thermochemical parameters T , c , d , crustal properties V_s , V_p , ρ , d_{cr} , or anisotropy parameters ξ , ϕ , η was randomly selected, and subsequently, all parameters in the set were perturbed using the prior distribution as defined in section 4.2. The adopted distribution was found to have a burn-in time (number of iterations until samples were retained from the posterior distribution) of $\sim 10^4$. In all we sampled 1 million models and to ensure near-independent samples every 100th

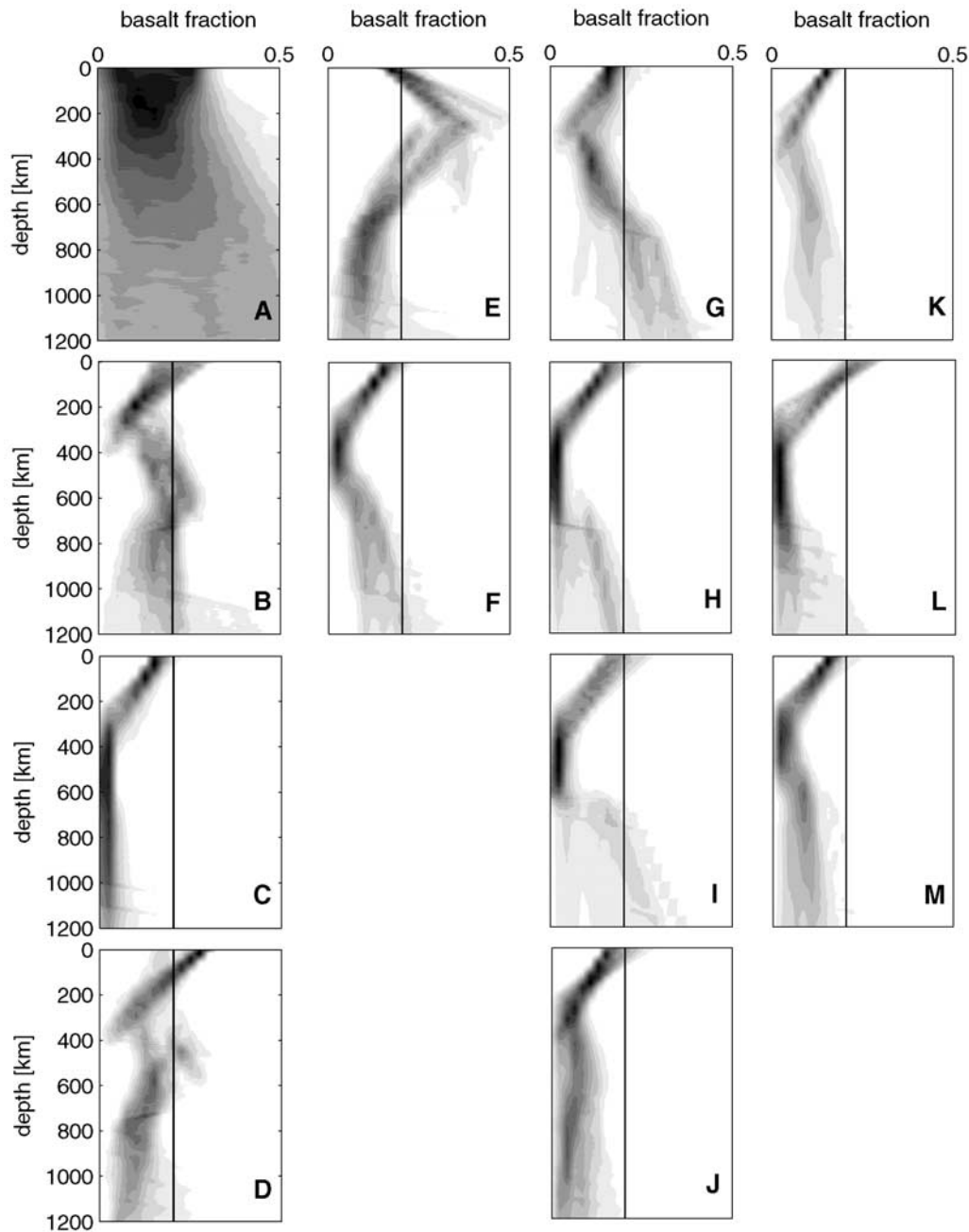


Figure 3. Marginal posterior models of bulk chemical composition (basalt fraction) as a function of depth. (a) Sampled prior information for comparison. (b–m) Solid vertical line indicates composition of pyrolite in NaCFMAS components for locations B–M on the map in Figure 1. At each kilometer a histogram of the marginal probability distribution of sampled basalt fraction was determined and by lining up these marginals, basalt fraction as a function of depth is envisioned as contours directly relating their probability of occurrence. The contour lines define eight equally sized probability density intervals for the distributions, with black most probable and white least probable.

model was retained for further analysis, with an overall acceptance rate of about 30%.

5. Results and Discussion

5.1. Calculated Data

[35] Figure 2 shows a typical fit to data, illustrated using a location in the Indian Ocean at 90°E, 0°N. All Rayleigh and

Love wave branches are seen to be fit within the uncertainties given by *Visser et al.* [2008a].

5.2. Mantle Composition

[36] The compositional variation for each location is shown in Figure 3. The vertical line in Figures 3a–3m indicates the value representative of the pyrolite composition obtained from a recent geochemical estimate of the Earth's primitive upper mantle (PUM) composition (hypo-

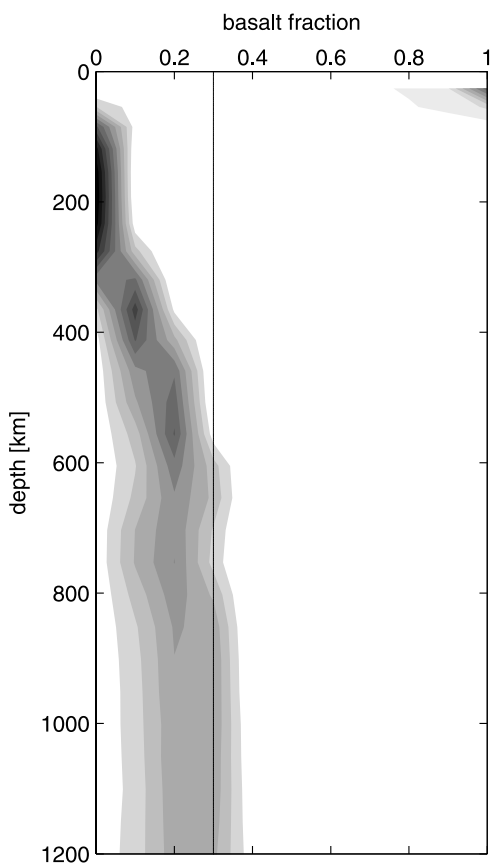


Figure 4. Probability map of basalt fraction as a function of depth compiled from the geodynamical study of Nakagawa *et al.* [2009]. Solid vertical line indicates the bulk composition in CFMAS components equivalent to pyrolite. Shades of gray as in Figure 3.

thetical composition of the mantle before the basaltic crust has been extracted, but after the core has formed) by Lyubetskaya and Korenaga [2007].

[37] While the compositions shown in Figure 3 are seen to differ in detail among different locations, there are some first-order trends that stand out. For instance, and excepting the Russian craton, all sites show a decrease in basalt fraction from a generally pyrolitic value in the first 300–400 km of the upper mantle, followed by either an increase in or a constant value of basalt fraction throughout the transition zone (TZ) and into the upper part of the lower mantle. In particular, the constant-composition scenario throughout the TZ is seen to be often recurring. For the most part, all locations remain on the harzburgite-rich side of the pyrolite composition down to and below the TZ. Excepting the Indonesian site, almost all locations, within the range of the models sampled, display an increase in basalt fraction that either approaches a pyrolitic mixture or increases to a basalt-rich composition for depths below ~800–1000 km. At C (Indonesia), which is located close to a subduction zone, the harzburgite-rich composition persisting well into the upper part of the lower mantle could be related to slab penetration of the lower mantle. Evidence in support of the latter scenario also comes from seismic tomography studies that shows the presence of a large-scale slab that runs roughly from Anatolia to the Pacific

[e.g., Van der Hilst *et al.*, 1997; Grand *et al.*, 1997; Boschi and Dziewonski, 1999].

[38] With regard to the somewhat anomalous composition that we obtained for the location beneath the Russian platform, we investigated another cratonic site centered on the Canadian shield (not shown), and found mantle compositions and geotherms that resembled those obtained for the location around the western margin of North America (site F in Figure 1). This observation does not explain the anomalous character of site E, and only further analysis of other cratonic sites will be able to determine whether the current petrological model can adequately explain regions such as the old continental lithosphere.

[39] The results presented here are not only indicative of lateral as well as depth-dependent chemical variations, but also of significant deviations from pyrolite. The harzburgite-rich nature of our compositional profiles throughout the upper mantle and transition zone agrees with asthenospheric melting at mid-ocean ridges [Ringwood, 1975]. Moreover, the dynamical process by which slabs become chemically segregated as they penetrate into the deeper mantle [Xie and Tackley, 2004], not only provides a mechanism for generating mantle heterogeneities, but also for producing the observed increase in basalt in the mid-to-lower mantle.

[40] In support of these processes and the results presented here, we have compiled compositional profiles taken from a recent numerical modeling study by Nakagawa *et al.* [2009], which combines self-consistently calculated mineral physics parameters with thermochemical 3-D mantle convection simulations. T. Nakagawa kindly extracted some 25000 radial compositional profiles at evenly distributed locations over the sphere. The profiles are shown in Figure 4 as a probabilistic map of basalt fraction as a function of depth, and in spite of their use of a simpler (CFMAS), but higher-resolution (more depth nodes), chemical model, also point to the main features seen in our results, i.e., basalt depletion and enrichment of the upper and mid-to-lower mantle, respectively. Note that these geodynamical models encompass a wide range of basalt fractions in and below the TZ, with values ranging from very harzburgite-rich to harzburgite-poor and thus overlap the range of basalt fractions found here. The two-component model employed here and by Nakagawa *et al.* [2009], based on distinct end-members, is found to provide an adequate description of the geophysical data.

[41] Other evidence for a compositional gradient comes from recent work by Cammarano *et al.* [2009]. Rather than considering data, they invert seismic tomography models from other studies to map out global thermal variations in the upper mantle and TZ using the mechanical mixture approach of Xu *et al.* [2008]. Assuming various fixed compositions from pyrolite over harzburgite to more enriched models, Cammarano *et al.* consistently find geotherms with negative thermal gradients around the major phase transitions. On the basis of these, it is argued that for a given negative geotherm to become positive a gradual change to more enriched compositions is required.

[42] As discussed in section 3.2, Xu *et al.* [2008] consider the mantle to be made up of a nonequilibrium mechanical mixture of the two end-member components. Their analysis suggests a radial gradient in the basalt fraction, in agreement with present findings, as models with basalt depletion in the

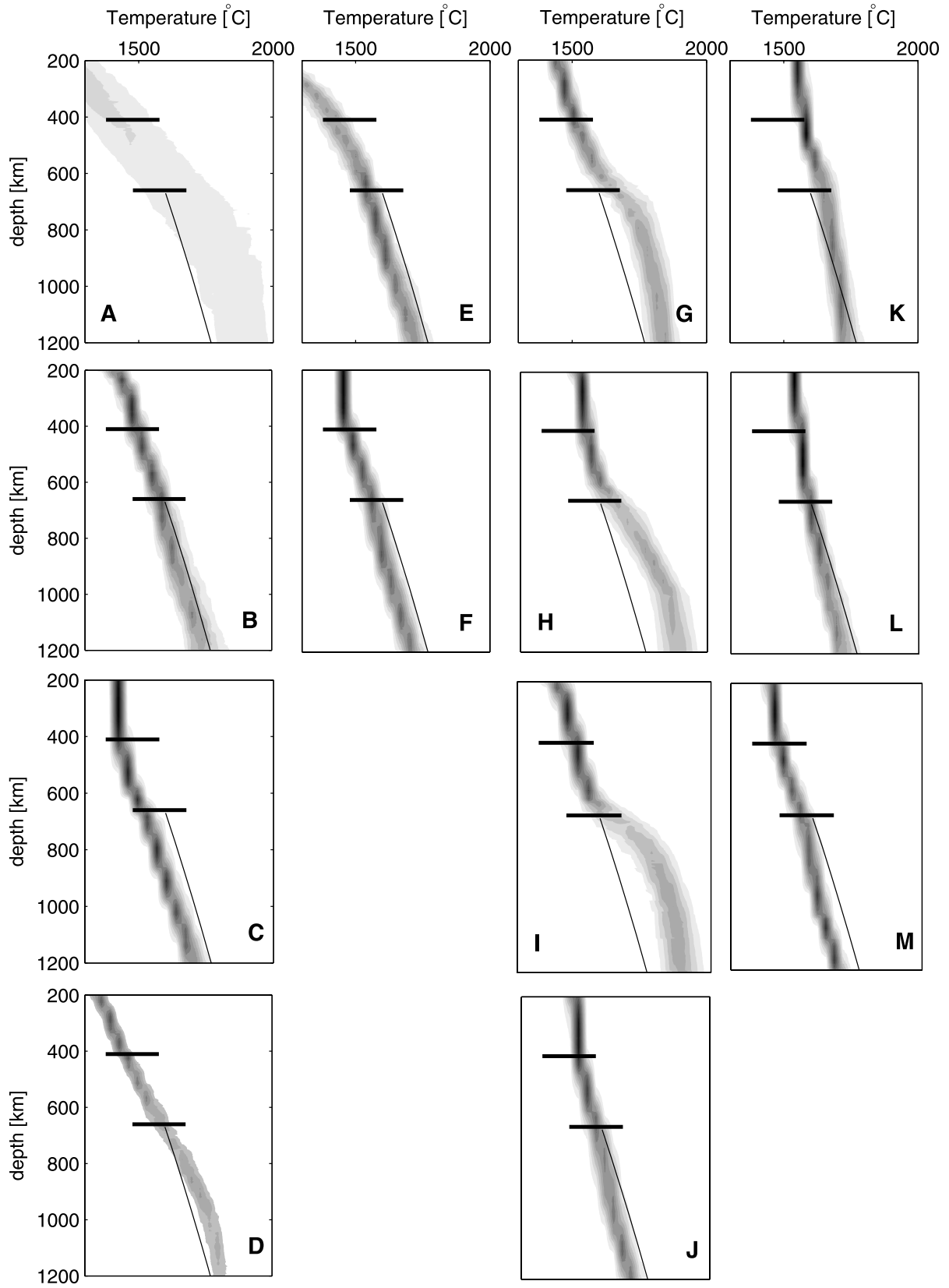


Figure 5

upper mantle and enrichment in the upper part of the lower mantle, respectively, were found qualitatively to be in better accord with PREM and AK135. To test this in a more quantitative fashion, we singled out a locality in the Pacific Ocean (site H in Figure 1) and reinverted data using the mechanical mixture approach of Xu and coworkers. We found overall that the results so obtained differed only to a minor extent from those where the assumption of equilibrium assemblage was made. While essentially no differences in mantle geotherms (see section 5.3) were found, only small variations in detail between the two mantle compositions were observed. Throughout the depth range 300–1200 km, the composition for mechanical mixture, as in the case of equilibrium assemblage (Figure 3h), remained on the harzburgite-rich side of pyrolite.

[43] As a test of the robustness of our results we singled out several locations and reinverted data at these particular sites with a fixed pyrolite composition, leaving all other parameters variable. As a result of this we observed a deterioration in data misfit, to the extent that longer period data along higher mode branches could no longer be fit within uncertainties.

5.3. Mantle Geotherms

[44] Mantle geotherms are displayed in Figure 5, and as in the case of composition, geotherms among the different locations vary. Constraints on the upper mantle geotherm come from mineral phase transitions measured in the laboratory. For example, if the 410 and 660 km seismic discontinuities (hereinafter referred to as the 410 and the 660) correspond to the olivine (Ol) → wadsleyite (Wad) and ringwoodite (Ring) → magnesio-wüstite (Mw) + perovskite (Pv) transformations, then the temperature at these depths can be inferred to be $\sim 1750 \pm 100$ K and $\sim 1900 \pm 150$ K, respectively [Ito and Takahashi, 1989]. In addition, we also show the “adiabatic” geotherm determined by Brown and Shankland [1981].

[45] Lateral as well as depth-dependent variations in mantle temperature are recognizable in Figure 5, in particular, with regard to variations among the different geological settings. A clear example involves TZ temperatures, notably at the 410 and 660. Continental and cratonic sites are overall colder, by up to as much as 100°C than their oceanic and oceanic ridge counterparts. In the upper part of the lower mantle differences are even more striking, although no clear trends are visible. It appears that lower mantle temperatures for continental (B and C) and cratonic sites (E and F) are subadiabatic, whereas a notable feature of most oceanic sites (G–I) is the superadiabatic lower mantle. For the ocean ridges (K–M) this trend is reversed and most of these sites are subadiabatic. The three superadiabatic oceanic sites (G–I) are also distinguishable by the presence of a thermal boundary layer (TBL) just beneath the transition to the lower mantle, which seems

to be related to the rather abrupt change in chemical composition occurring between upper and lower mantle as is evident in Figures 5g–5i. None of the other sites suggest such sudden changes in chemistry, and therefore also no TBL.

[46] In a recent study, Ritsema *et al.* [2009] have employed the approach of Xu *et al.* [2008] to map potential temperature in the transition zone beneath the Pacific and circum-Pacific by modeling travel time differences of shear wave reflections off the 410 and 660 km. Under gross simplifying assumptions, such as fixing basalt fraction (bulk chemistry is pyrolitic) and considering only adiabats, Ritsema *et al.* vary mantle potential temperatures for a mechanical mixture from 1400 to 1800 K and find the lowest temperatures in the western Pacific region, while the highest temperatures are found in the central Pacific, in overall agreement with present results. Differences between cratonic and oceanic geotherms were also found by Cammarano and Romanowicz [2007], who inverted long-period seismic waveforms for global 3-D thermal variations in the upper mantle. Using the mineral physics database of Stixrude and Lithgow-Bertelloni [2007] and a constant bulk pyrolitic composition, temperature differences between cratons and oceans in the TZ easily attained values of 100°K .

[47] Physical structure of the transition zone, in particular TZ thickness, is found to be mostly controlled by temperature and only to a lesser extent by composition. This is exemplified in Figure 6, which shows the phase equilibria for a “cold” (Figure 6a) and a “hot” (Figure 6b) geotherm calculated on the basis of a constant pyrolite composition. Effects of olivine phase transitions on shear wave velocities are clearly visible, which result in major velocity discontinuities at the locations at which the transformations Ol → Wad (the 410) and Ring → perovskite (Pv) + Mw (the 660), and to a lesser extent Wad → Ring (the 520), take place. The effects of temperature are clearly visible; relative to the cold geotherm the phase transformations from Ol to Wad and Ring to Pv + Mw move down and up, respectively, leading to a thinner TZ under warm conditions. An additional reaction of the system is the behavior of the 520; along a hot geotherm the transformation gets drawn out leading to a more smoothly varying *S* wave velocity across the transition.

[48] Adding changes in composition on top of thermal perturbations potentially complicates the above interpretations, although in the examples shown here (Figures 6c–6d), the correlation of TZ thickness with temperature is replicated, with marked changes occurring for the 410. Figures 6c and 6d show phase equilibria for the case of a compositional gradient extending throughout the mantle (basalt fraction increases linearly from 0.15 to 0.35), using the same hot and cold geotherms as in Figures 6a and 6b, respectively. The complexity is born out in the behavior of

Figure 5. (b–m) Marginal posterior models of temperature as a function of depth. (a) Sampled prior information for comparison for locations B–M on the map in Figure 1. Experimentally determined temperatures for the reactions olivine → wadsleyite (solid horizontal line at 410 km depth) and ringwoodite → magnesio-wüstite + perovskite (solid horizontal line at 660 km depth) have also been included for comparison (see main text for further discussion). The width of the bars indicates experimentally determined uncertainties. Thin solid line is the geotherm from Brown and Shankland [1981]. Shades of gray as in Figure 3.

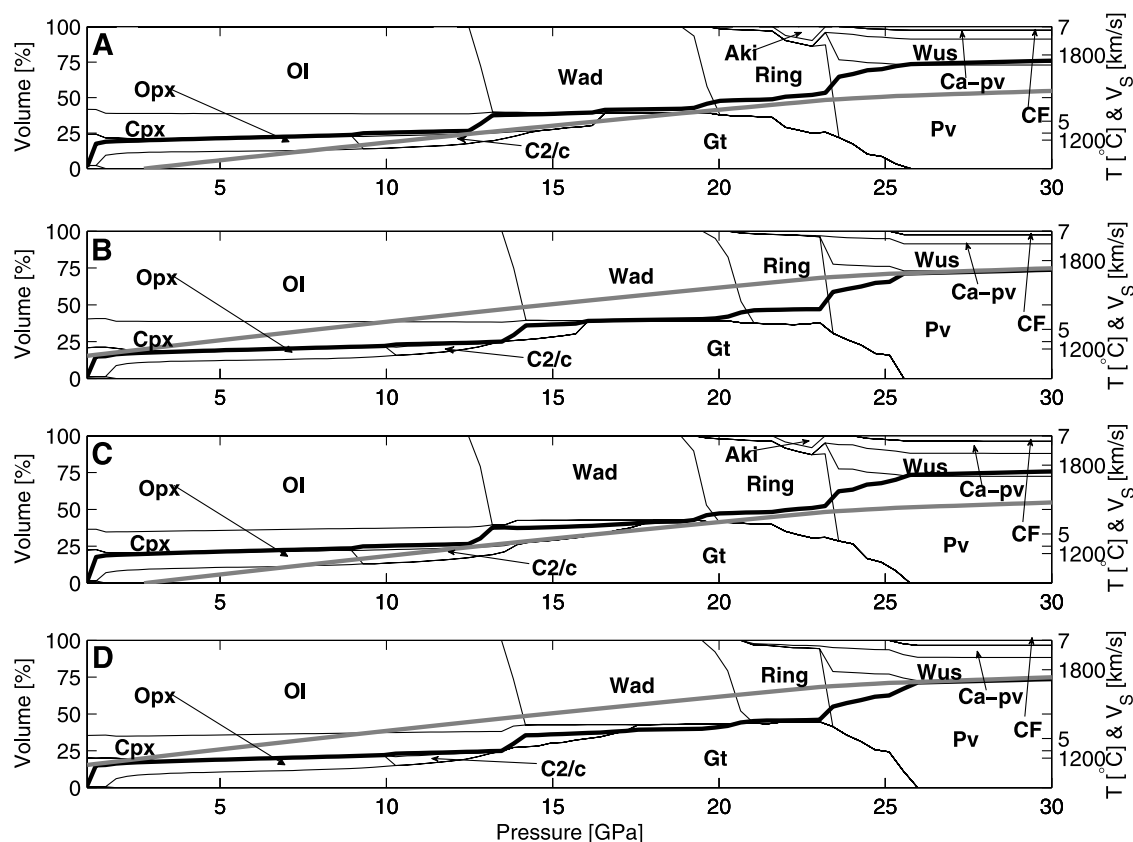


Figure 6. Variations in phase proportions and shear wave velocity (thick black lines throughout) in the pressure range 0 to 30 GPa (surface to ~ 750 km depth) calculated for (a) a cold geotherm (thick gray lines) and constant pyrolitic composition, (b) a hot geotherm and constant pyrolitic composition, (c) a cold geotherm and depth-dependent bulk composition (linear gradient in basalt fraction with depth), and (d) a hot geotherm and similar composition as in Figure 6c. Phases are OI (olivine), Opx (orthopyroxene), Cpx (clinopyroxene), C2/c (high-pressure Mg-rich Cpx), Gt (garnet), Wad (wadsleyite), Ring (ringwoodite), Aki (akimotoite), Ca-Pv (calcium perovskite), Mw (magnesiowüstite), Pv (perovskite), and CF (calcium ferrite).

the 660; even in the case of the cold geotherm/changing composition, the 660 moves up rather than down relative to the hot geotherm/constant pyrolite case. Note also the appearance of structure in the 660 in the form a secondary jump in shear wave velocity around 26–27 GPa, depending on the abruptness of the transformation of garnet (Gt) to Pv. Relatively hot conditions tend to favor a shorter transition interval for the transformation of Gt, whereas this is not seen in the case of the cold geotherm. Here the transformation of Gt proceeds smoothly as does the accompanying shear wave velocity increase.

[49] That TZ structure, in general, is mainly controlled by temperature is reflected in the behavior of the 410 discontinuity. For the locations where relatively cold temperatures in the upper part of the TZ are found (continents and cratons), the 410 moves up (on average to ~ 400 km depth), while for ocean and ocean ridge sites, with relatively high temperatures in the upper TZ, the 410 typically occurs deeper (around 420 km depth). With regard to TZ thickness, our results are in broad agreement with previous studies of transition zone structure [e.g., *Flanagan and Shearer*, 1999; e.g., *Gu and Dziewonski*, 2002; *Lawrence and Shearer*, 2006] that found, within the small differences of the models, the central Pacific, mid-ocean ridges in the Atlantic, and

Indian Ocean to have thinner TZ thicknesses, while continental and cratonic sites have thicker TZ thicknesses. Precise agreement is not warranted here as surface wave data are not as sensitive to the exact location of discontinuities as are converted or reflected phases, for example.

[50] To test the overall sensitivity of the thermal variations, we considered a number of locations and fixed the geotherm to the adiabat of *Brown and Shankland* [1981] and reinverted the surface wave dispersion data, with the result that a number of branches could no longer be fit. This points up the importance of thermal contributions in addition to those arising from composition.

[51] As we presently discount effects arising from attenuation, notably dispersion, which tends to reduce velocities, we are potentially disregarding a mechanism other than temperature that acts to lower velocities. In order to test this, we considered a site where inverted mantle temperatures are found to be relatively high, such as in the western part of the Pacific Ocean (location G in Figure 1), and reinverted data for this location assuming attenuation to be a thermally activated process as considered by, e.g., *Karato* [1993] and using data for polycrystalline olivine measured by *Jackson et al.* [2002]. As expected the resulting temperature profiles from this inversion were found to be somewhat cooler

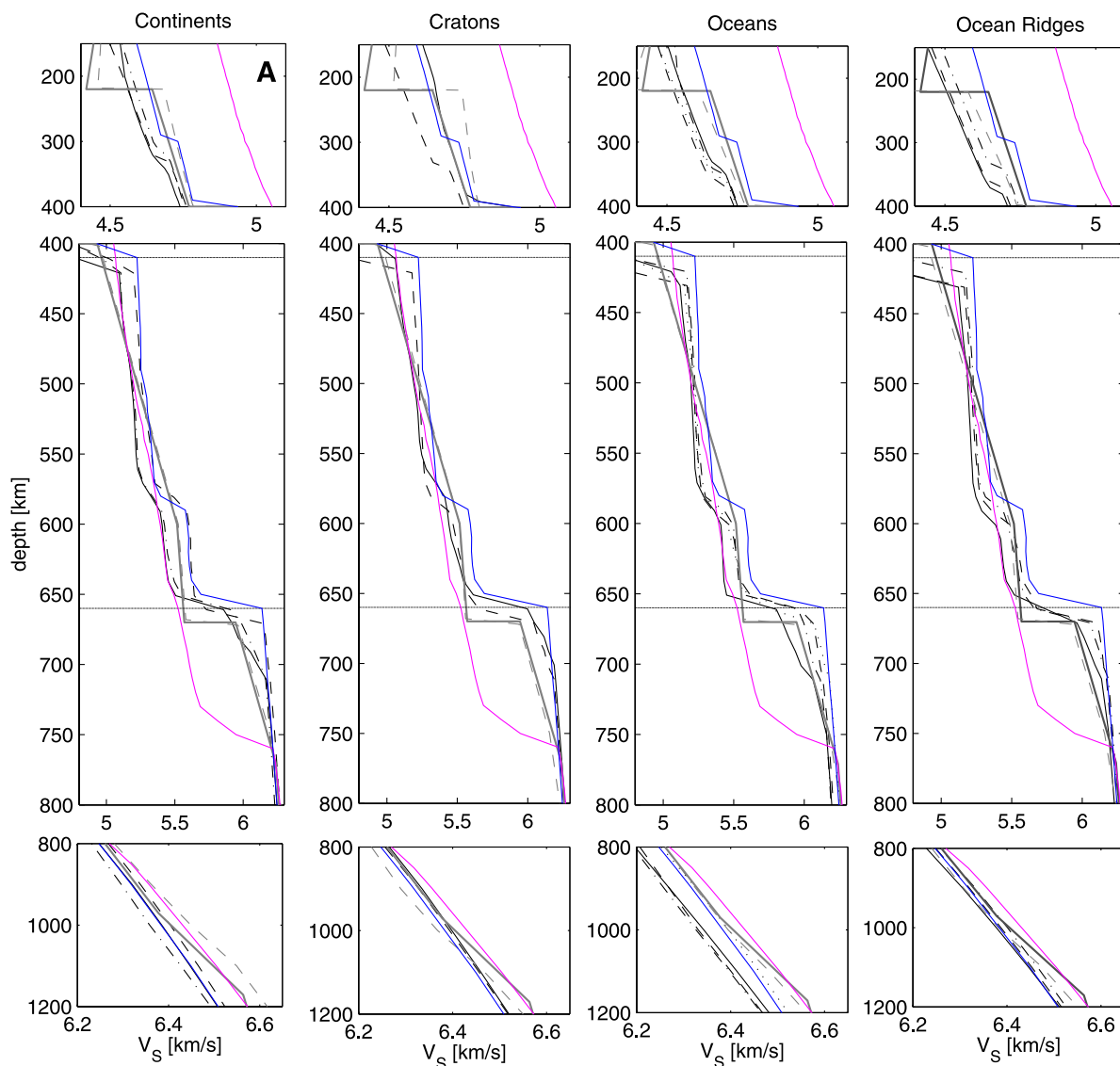


Figure 7. Variations in mantle isotropic physical properties. (a) S wave velocity, (b) P wave velocity, and (c) density. Models in each column are ordered according to geological setting, with the following nomenclature for all plots: PREM (solid gray), SMEAN/vox5p07/SPRD6 (dashed gray), basalt (magenta) and harzburgite (blue). Our results are represented by lines of different style, depending on location and general tectonic setting: “Continents”: 30°E, 0°N (solid), 120°E, 0°N (dashed), 75°W, 0°N (dot-dashed). “Cratons”: 60°E, 60°N (solid), 114°W, 44°N (dashed). “Oceans”: 90°E, 0°N (solid), 165°E, 0°N (dashed), 165°W, 0°N (dot-dashed), 135°W, 0°N (dotted). “Ocean ridges”: 105°W, 0°N (solid), 20°W, 65°N (dashed), 0°E, 57°S (dot-dashed). Note that for models SMEAN/vox5p07/SPRD6, only the average model for each tectonic region is shown.

relative to those shown in Figure 5g (composition essentially remained unchanged). However, and in spite of the apparent contribution of attenuation to mantle temperatures, we nonetheless consider it premature given the very few measurements available to constrain attenuation at mantle conditions, and for the reasons discussed at the end of section 3.2, to incorporate attenuation in the present study.

5.4. Isotropic Physical Properties

[52] Derived physical properties in the form of seismic P and S wave velocities and densities are shown in

Figures 7a–7c for the depth range where most of the variation occurs, i.e., from 150 to 1200 km. However, rather than showing all sampled models, which would tend to obscure details, we only plotted mean physical properties, after having verified that the posterior pdf’s for these parameters were generally gaussian shaped. Uncertainties are ± 0.1 km/s, ± 0.14 km/s and ± 0.03 g/cm³ for V_s , V_p and ρ , respectively. For comparison we are also showing PREM and the means of seismic tomography models vox5p07, SMEAN and SPRD6, in addition to physical properties calculated self-consistently for basalt and harzburgite end-member model compositions along the geotherm of *Brown*

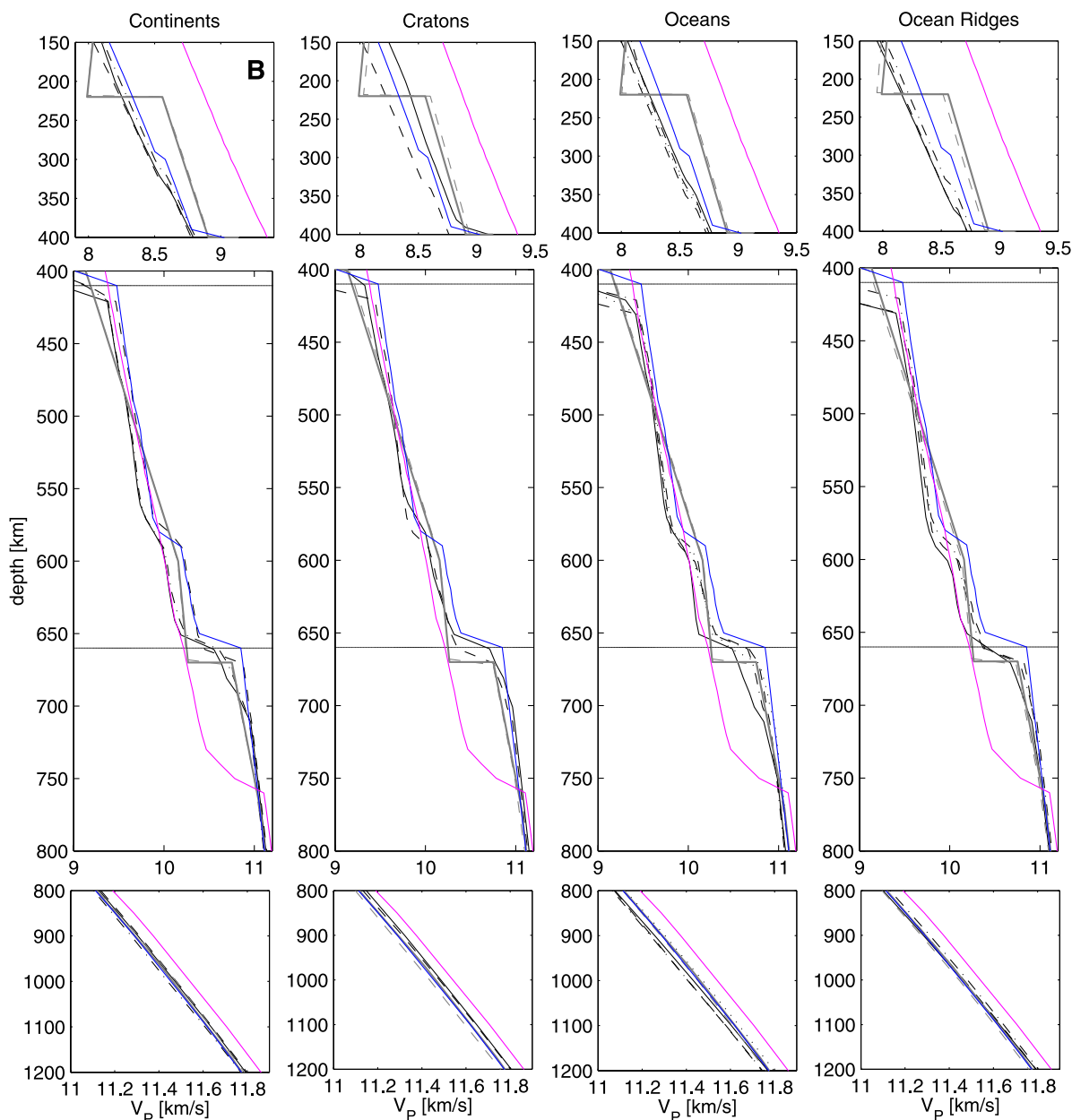


Figure 7. (continued)

and Shankland [1981]. vox5p07 is a P wave velocity model that Boschi *et al.* [2008] derived with Boschi and Dziewonski's [1999] method, inverting Antolik *et al.*'s [2001] improved database, based on P , PKP and PcP traveltimes observations from the International Seismological Centre (ISC) bulletins. vox5p07 is parameterized with 15 layers of equal-area (5×5 degrees at the equator) pixels. The model SMEAN was derived by Becker and Boschi [2002] as an average of a number of seismic tomography models. SMEAN was found to match geodynamical [Steinberger and Calderwood, 2006] and seismological [Qin *et al.*, 2009] observables at least as well as most recently published tomographic models. The long-wavelength density structure is contained in model SPRD6, which is based on a large collection of normal-mode data and free-air gravity constraints [Ishii and

Tromp, 1999]. From Figures 7a–7c the relatively strong correlations of SMEAN and vox5p07 and SPRD6 with PREM are apparent and stem from the choice of the latter as reference model. The seismic tomography models are essentially derived as small perturbations with respect to PREM and typically adopt its parameterization, in particular the 410 and 660, with little independent determination.

[53] Features that here appear to be robust are on average higher velocities than PREM and SMEAN/vox5p07 in the upper mantle from 150 km and down to the 220 discontinuity at which point PREM becomes faster than our models. Cratons are on average faster than continents, and both are faster than oceans and ocean ridges. In the depth range ~ 330 – 370 km velocities derived here increase slightly due to the transformation of orthopyroxene (Opx) to high-

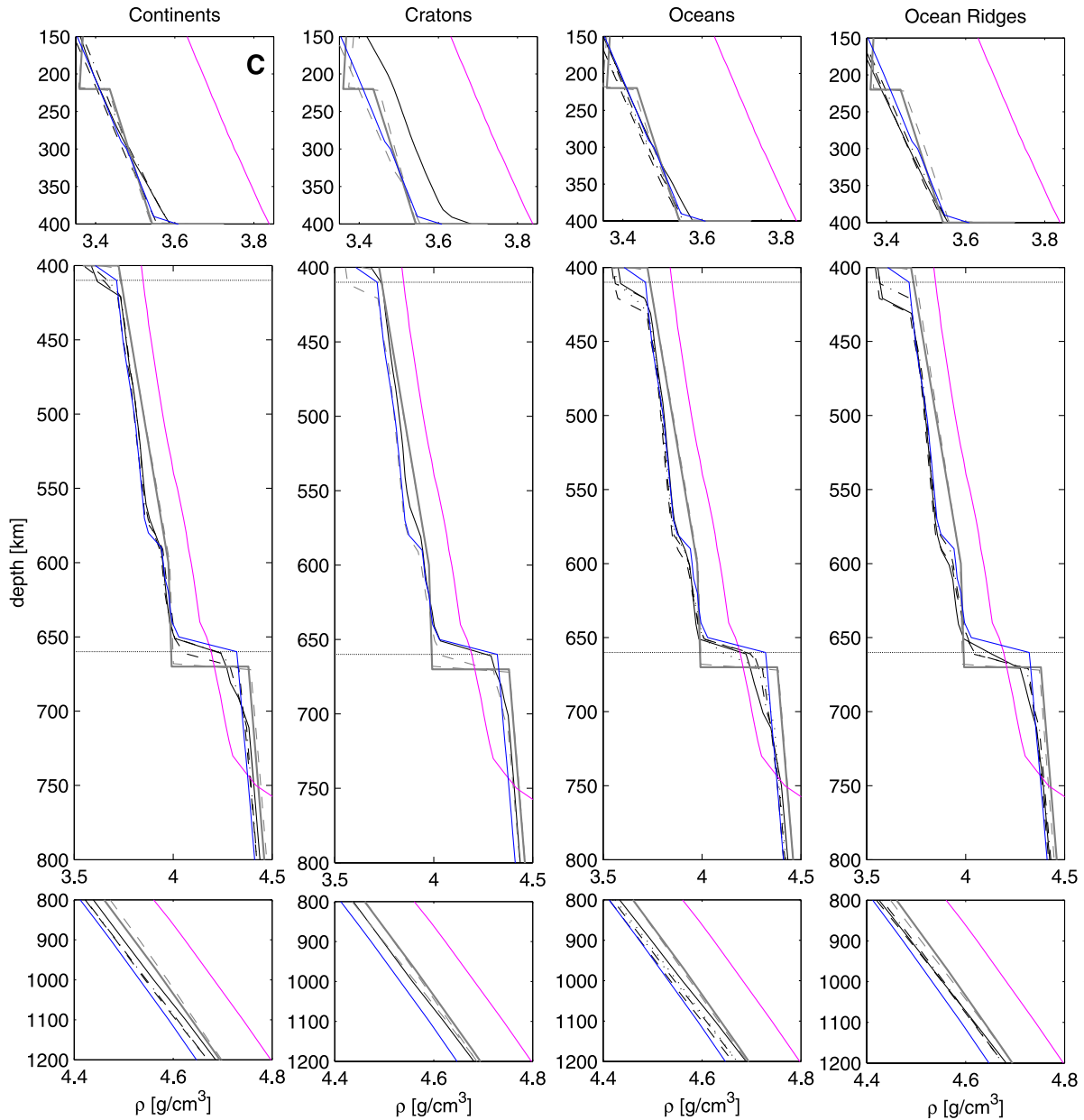


Figure 7. (continued)

pressure Mg-rich clinopyroxene (C2/c) but remain on average slower than PREM down to ~ 410 km depth. These upper mantle features agree with results from previous tomography models [Panning and Romanowicz, 2006; Kustowski et al., 2008; Nettles and Dziewonski, 2008]. Densities exhibit much the same behavior just described for P and S wave velocities, with the exception that densities, for continents and cratons in particular, appear on average to be higher than in PREM and SPRD6 from 300 km down to ~ 410 km depth. In the upper half of the TZ P and S wave velocities are found to be higher than PREM and SMEAN/vox5p07, while in the lower part P and S wave velocities are slightly lower than PREM and SMEAN/vox5p07, implying an overall steeper velocity gradient in this region. An additional transition to higher velocities below the 660 extending down to ~ 750 km depth is observed here. The density profiles, meanwhile, are all less

dense than PREM and SPRD6 in the upper to mid-TZ, i.e., in-between the transformations $\text{Ol} \rightarrow \text{Wad}$ and $\text{Wad} \rightarrow \text{Ring}$. At the latter, densities increase to the extent that they reach PREM, while below the TZ densities again become less than PREM. Another striking feature of our models is the magnitude of the 410 relative to previous seismic models, with PREM, SMEAN and vox5p07 all having smaller 410s, while the 410 in SPRD6 is of the same magnitude as in our density models. The size of the 410 in our models can be reduced by considering compositional models with increased Ol depletion in the upper mantle as proposed by Duffy et al. [1995]. In particular, the jump in our models matches PREM by increasing basalt fraction to ~ 0.45 locally in contrast to what is found here where only a single site suggests such high enrichments in the basaltic component in the upper mantle. However, as the data considered here are less sensitive to location and size of

discontinuities, we leave it for future studies to investigate this discrepancy in detail.

[54] The seismic discontinuity associated with the Wad \rightarrow Ring phase transformation (the 520) is not present in PREM nor in any of the tomography models shown here, but is seen to be a consistent feature of our models and must be globally present. The transition here occurs deeper than 520 km depth, around 560–580 km, and is generally not very large. From Figure 6 we observe that relatively hot conditions tends to draw out the transition, while adding a compositional gradient renders it almost smooth and thus undetectable, which might explain why it defies detection on a global scale [Deuss and Woodhouse, 2001]. Looking at precursors of SS waves, which are shear waves that initially travel downward away from the source, then turn back up, and are reflected off of the 520, Deuss and Woodhouse also observed double reflections at several locations from depths of 500–515 km and 550–570 km, respectively. The latter generally agrees with what we find here, whereas there is no evidence for the former. Although the reflections from 500 to 515 km depth could possibly be attributed to transitions in the non-Ol component, in particular C2/c \rightarrow Gt, they are probably much too weak to account for the observations.

[55] For the depth range 700–1200 km, differences between physical properties derived here and PREM and SMEAN/vox5p07 generally become much smaller as also observed by Kustowski *et al.* [2008] for example. For the most part, P and S wave velocities are either equal to or slightly slower than PREM and SMEAN/vox5p07, while densities are overall less dense than PREM and SPRD6.

[56] First-order interpretations of the main TZ features in terms of compositional and thermal effects is facilitated by comparison with our calculated basalt and harzburgite profiles (hereinafter referred to as M and H, respectively) and the observation that our inverted velocities are not always bracketed by the limits defined by the M and H end-members. One observes immediately that M is generally devoid of structure throughout the TZ with no 410, because of the absence of Ol and transformations to its higher-pressure phases Wad and Ring. Moreover, features present in H broadly resemble those in our models. For example the 410 in H almost coincides with that in PREM, but the jump is larger and resembles more the discontinuity of our models. Because of the absence of a 410 in M, the only way to move it up or down would be to either increase or decrease the temperature at the top of the TZ. This explains the harzburgite-rich nature of our models in the upper mantle as well as the observed temperature variations. For the oceanic and oceanic ridge locations one observes that throughout the middle to lower part of the TZ (500–580 km) both M and H, like PREM, are faster than our models. The only way then to decrease velocities further would be to increase temperatures. The 660 transition is seen to occur at around 650 km depth in H and at around 725 km in M, while in our models it occurs between 650 and 670 km depth. In addition, velocities predicted for, as well as beneath, the discontinuity in our models are not as fast as those predicted by H, which is probably more difficult to achieve through a change in either composition or temperature alone.

[57] Although we would like to note that the above examples are based on simple visual inferences, the dis-

cussion raises the issue of parameter trade-off, i.e., that a given feature can be produced by either changing composition or temperature for example. In order to verify that this is not the case we have investigated the correlation that exists among basalt fraction and temperature for all locations throughout the depth range of interest. In Figure 8 we show examples for two locations that reveal the overall uncorrelated nature of these parameters.

5.5. Radial Anisotropic Structure

[58] As mentioned, surface wave studies have shown that strong lateral and radial variations exist in the upper mantle. Moving beyond the lithosphere-asthenosphere system, Panning and Romanowicz [2004, 2006] for example, reported significant anisotropic variations in TZ as well as in D'' , with the lower mantle predominantly characterized by a horizontal flow pattern, and deviations from these at superplumes. However, while several recent studies [e.g., Boschi and Dziewonski, 2000; Panning and Romanowicz, 2006; Kustowski *et al.*, 2008; Visser *et al.*, 2008a, 2008b] indicate the presence of some form of radial anisotropic variations throughout the mantle, they only tend to agree at long wavelengths as pointed out by Panning and Romanowicz [2006] and Kustowski *et al.* [2008]. On the basis of correlation tests, Kustowski *et al.* concluded that anisotropic variations are consistent only at 150 and 2800 km depth. The latter authors also went on to test the robustness of their whole mantle anisotropic model by specifically comparing improvement in data fit between a model with anisotropy extending to 400 km depth, and a whole mantle anisotropic model. The comparisons revealed only little improvement in data fit for the latter model over their preferred model where anisotropy is confined to the upper mantle. These tests suggest that the presence of radial anisotropy in the middle and lower mantle is not a robust feature. The large uncertainties in these models could be related to differences in inverse and regularization method employed, the specific parameterization invoked and/or the particular data set investigated, of which the latter has been addressed by Carannante and Boschi [2005].

[59] Plots of radial anisotropic structure beneath each location are shown in Figure 9. For comparison, we are also showing some previous results in the form of PREM and three global 3-D anisotropic models from the studies of Panning and Romanowicz [2006], Visser *et al.* [2008a], and Kustowski *et al.* [2008]. All locations investigated here show positive shear wave anisotropy in the upper mantle, with strong regional differences in peak amplitudes. Most locations peak in the depth range 50–150 km, with the maximum amplitude generally occurring at \sim 100 km depth and thus concur with previous studies as regards the positive anisotropic signature of the upper mantle, and significant differences from PREM. For comparison, Kustowski *et al.* [2008] found shear wave anisotropy to peak at 120 km depth, whereas in the models of Panning and Romanowicz [2006], maximum anisotropy generally tends to occur, much as in PREM, above 100 km depth. Figure 9 also reveals significant lateral variations in upper mantle anisotropy as suggested in many regionalized studies. In particular, we find relatively strong positive amplitudes in the depth range 100–150 km in the Indian Ocean and Pacific region with significant lateral variations, in

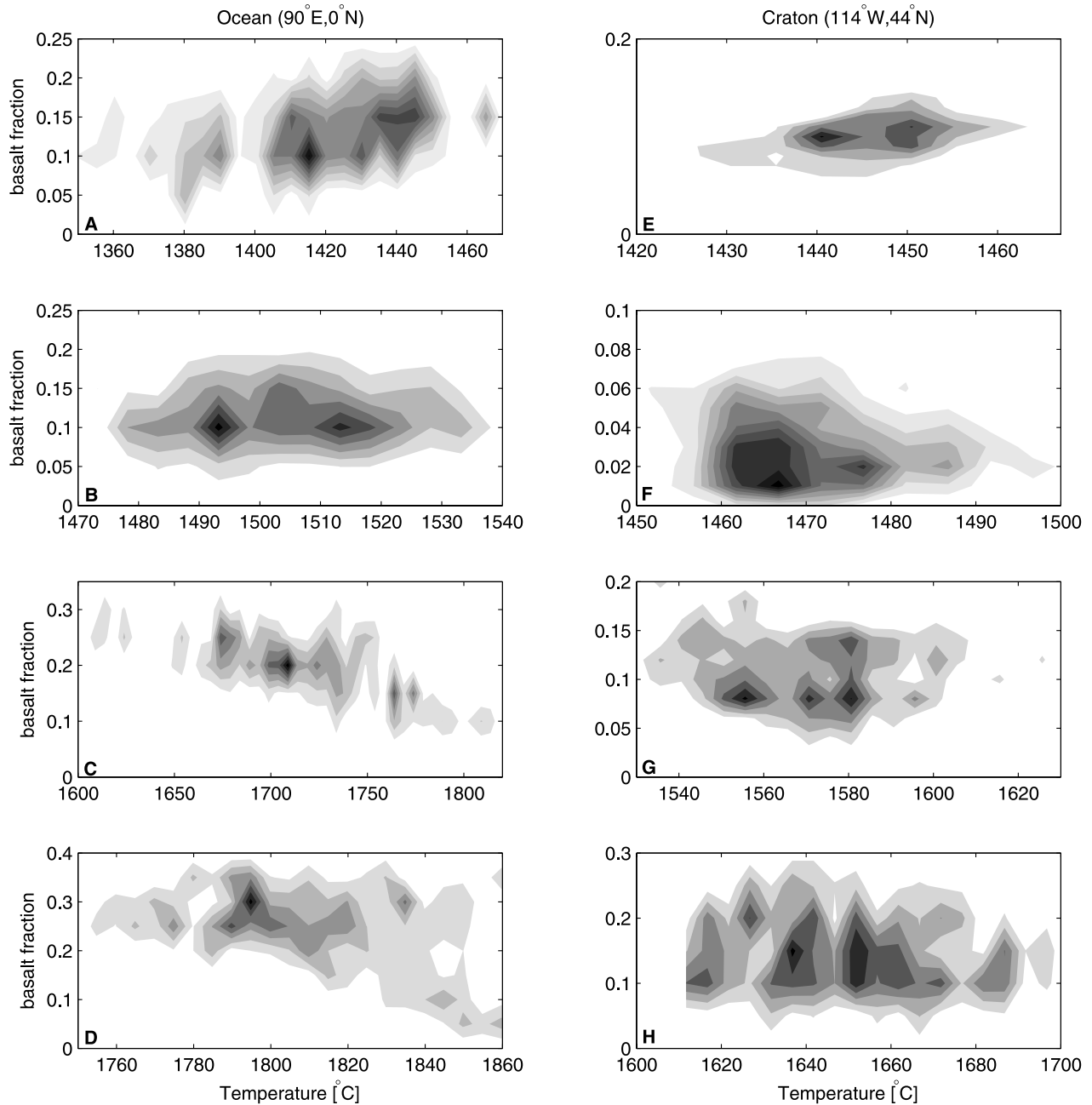


Figure 8. Two-dimensional marginal posterior probability density functions showing correlation between basalt fraction and temperature at two locations in the Indian Ocean (Figures 8a–8d) and over the North American craton (Figures 8e–8h) at depths in the mantle of (a and e) 150 km, (b and f) 400 km, (c and g) 700 km, and (d and h) 1000 km. Shades of gray are as in Figure 3.

agreement with the observations of *Ekström and Dziewonski* [1998] and subsequent studies. The anomalous anisotropy of the Pacific showed up as a reversal in sign of anisotropy between 80 and 150 km depth. However, given prior constraints on anisotropy employed here (see section 4.2.5), a change in sign of anisotropy at shallow depths will not be observed.

[60] Other locations showing a strong positive anisotropic signal are the continental and cratonic locations, in agreement with *Marone et al.* [2007] and *Kustowski et al.* [2008], although there are exceptions to these, in particular, beneath mid-Africa and the western part of the North American

continent. Apart from the latter two, other locations showing weak anisotropy are the ocean ridges, which are seen to differ from the previous models included here. A predominantly positive anisotropic signal beneath continents was reported by *Gung et al.* [2003] and is also observed here.

[61] The case for negative shear wave anisotropy in the depth range 200 to 600 km, as observed by *Panning and Romanowicz* [2006] and *Visser et al.* [2008b], does not seem to be substantiated here (except for the location over the Indian Ocean). That overall no change in sign of ξ is observed between upper mantle and TZ is partly a consequence of prior restrictions on ξ as can be seen in Figure 9a.

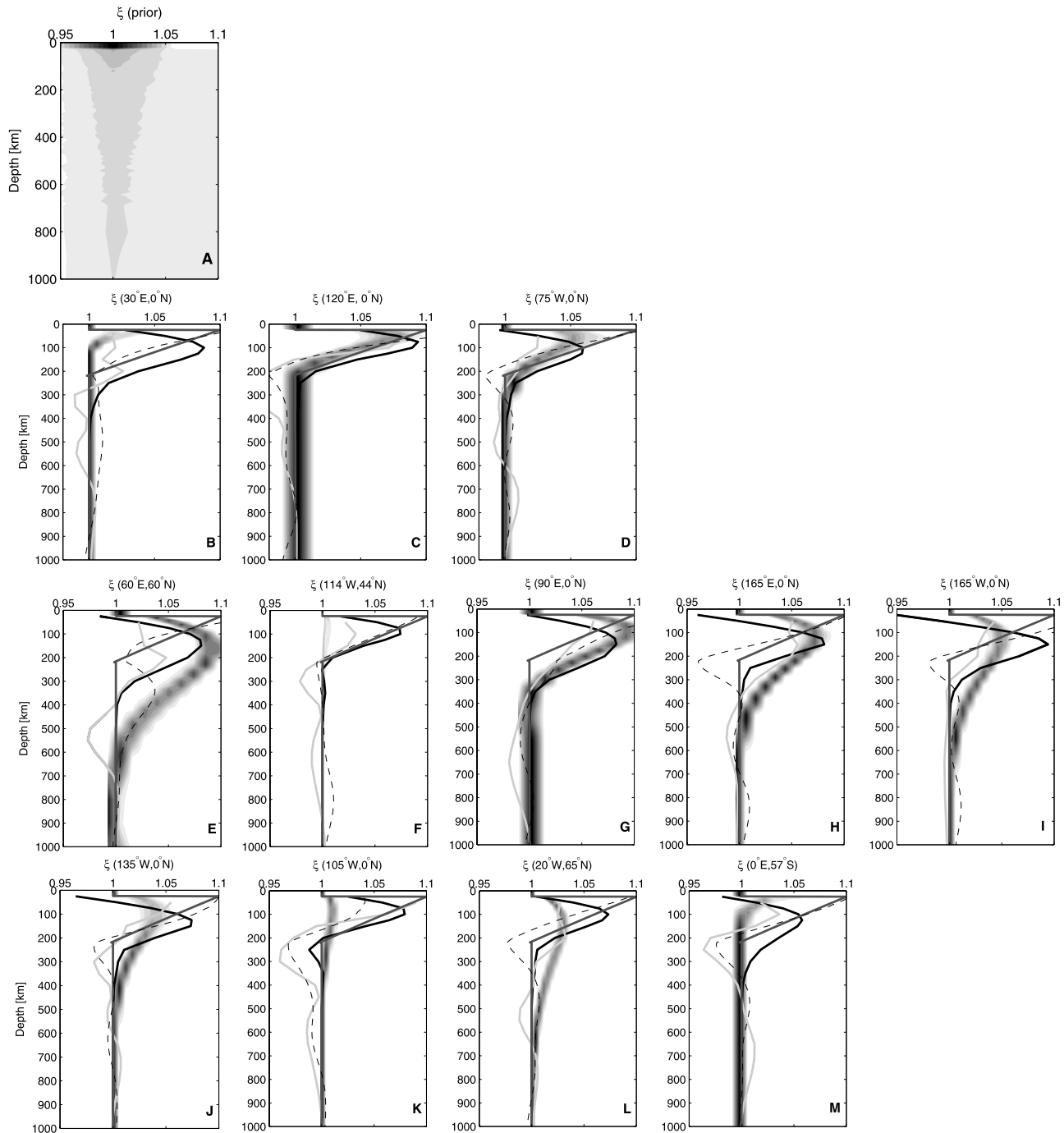


Figure 9. Marginal posterior probability density functions depicting 1-D radial anisotropy models at the various locations (shades of gray as in Figure 3). (a) Prior information and (b–m) locations in the map in Figure 1. In Figures 9b–9m, solid black lines are from the model of *Kustowski et al.* [2008], while light gray are from *Visser et al.* [2008b] and dark gray is PREM.

While Figure 9a shows that ξ a priori can be either >1 or <1 anywhere in the upper mantle, TZ, and upper part of the lower mantle, the nature of the anisotropy functionals employed here is such that because of their smooth form they tend to suppress the probability that significant sign changes occur as a function of depth. As a further technical note, we would like to point out that our results actually do indicate a change in sign of ξ , which, because of the binning when constructing histograms, is not observable. However,

as the observed sign change is very weak (ξ typically ranges from 0.992 to 1.0), we consider it negligible and for all intents and purposes as implying no change in anisotropy.

[62] Our results generally show signal amplitude to decrease in a continuous fashion as the transition zone is approached, such that anisotropy is no longer extant in the TZ. The upper part of the lower mantle at all locations investigated here appears to be isotropic and is thus in agreement with the preferred model of *Kustowski et al.*

[2008]. A glance at Figure 9 also reveals that the radial anisotropy models of *Panning and Romanowicz* [2006] generally disagree with the models of *Visser et al.* [2008b]. Only at possibly two locations do regions with $\xi < 1$ correlate (over the western Pacific and in the southern Mid-Atlantic Ridge). In particular, over the locations investigated here, *Kustowski et al.* [2008] do not find any evidence for a change of sign in radial anisotropy in the upper mantle, except for one location in the Pacific Ocean, and thus tend to follow the trend observed here. Below the TZ we find little evidence for anisotropy, in overall agreement with the preferred model of *Kustowski et al.* [2008].

[63] We further investigated the question of whether anisotropy in the TZ and mid-to-lower mantle is really required in order to simultaneously fit Rayleigh and Love wave data, by considering the case of an entirely isotropic mantle. Inversion of data at several locations revealed that while fundamental mode Rayleigh and Love wave dispersion curves could consistently not be fit, overtone branches generally fared better, although discrepancies in typically the first couple of overtones were nonetheless notable. The former is in accord with the consensus view of a strongly anisotropic upper mantle, whereas the apparent discrepancy of the latter might possibly indicate that anisotropy extends deeper, but that it is significantly weaker in comparison to the upper mantle.

[64] In order to verify the consistency of the overall positive radial anisotropy found here, we performed an inversion where we considered three of our locations and fixed radial anisotropy using the models of *Visser et al.* [2008b] for the same locations. What we observed was a general decrease in overall data misfit as a result. Causes for the discrepancies are thus to be found elsewhere and may be related to us jointly inverting both Rayleigh and Love wave data sets, rather than separately as done by *Visser et al.* [2008b]. Under the assumption of isotropy, they assumed that Love waves are sensitive to V_{sh} and Rayleigh waves to V_{sv} only and inverted these separately. This assumption is probably sufficient in the case of fundamental modes, but questionable for higher-order modes, as also noted by *Panning and Romanowicz* [2006] [see also *Anderson and Dziewonski*, 1982]. Discrepancies also relate to the particular inversion scheme used. *Visser et al.* [2008b] employed the neighborhood algorithm [*Sambridge*, 1999], and as this particular algorithm is only able to handle low-dimensional problems, the authors have taken further care to decrease the size of the model space to be searched by defining somewhat narrow bounds around a reference model (PREM). While the latter operation tends to linearize the problem, the former, and contrary to expectations, has not improved parameter resolution. Most parameters of *Visser et al.* [2008b] are generally poorly resolved.

[65] So far, discussion has centered on shear wave anisotropy, as data are mostly sensitive to this parameter. Although we also inverted for ϕ (P wave anisotropy) and η (see section 4.2.5), we do not show them here as they are not well constrained. Rayleigh and Love wave data are generally insensitive to ϕ , in particular, whereas η is more complicated as it is found to have an influence. As already mentioned, it has been the custom to fix η to its PREM value, where it is nonzero only in the upper 220 km. We

tested several different parameterizations of η and found that, while it does influence results to some extent, it is not to the extent of confusing the radial anisotropic signal, as also observed by *Ekström and Dziewonski* [1998]. As a result of this we follow *Kustowski et al.* [2008] and leave η variable, in spite of the fact that data are unable to constrain it and leave it for future studies using improved data to resolve η and ϕ .

[66] For the sake of completeness, we would like to note that possible trade-offs between anisotropic and compositional-thermal parameters were also investigated. All locations investigated showed no signs of any sort of correlation, which is what we would intuitively expect, given the independent nature of the two sets of fundamental parameters inverted for here. As a further example, correlations between, e.g., ξ and isotropic V_s were not observed either. We would like to point out that this does not necessarily exclude correlations between isotropic and anisotropic physical properties. However, the distinction between primary (e.g., T) and secondary parameters (e.g., V_s), which are conditional on the former, or even tertiary parameters (e.g., V_{sv} , V_{sh} , etc.) which depend on the values of both former parameters, should be made (for further discussion, see, e.g., *Bosch* [1999] or *Khan et al.* [2007]). Of importance here, and in general, are correlations among the primary parameters.

[67] Changes in sign of anisotropy are thought to indicate changes from horizontal to vertical flow under the assumption that anisotropy is the result of a preferred orientation of the crystal lattice of the anisotropic mantle minerals as these are subjected to strains due to mantle flow. This picture may however be complicated by the influence of pressure on the olivine dislocation creep, such that deformation of this part of the mantle may be dominated by diffusion creep instead as suggested by *Jung and Karato* [2001]. Diffusion creep unlike dislocation creep does not produce lattice preferred orientation of mantle minerals.

6. Conclusion

[68] We have combined a thermodynamic method with a rigorous nonlinear inversion scheme to infer lateral and radial variations in mantle temperatures, chemical composition and anisotropy at a number of locations spread across the globe and covering different geological settings. The thermodynamic method allows us to self-consistently calculate equilibrium mineralogy and bulk physical properties that are only functions of temperature, composition and pressure. Application of this method to discern mantle physical structure as done here, is different from standard seismic tomography methods, in that variations in V_s , V_p and ρ are naturally linked through the underlying common set of parameters. This not only results in sensitivity to all parameters simultaneously, but also allows us to naturally integrate vastly different data sets in an inversion.

[69] We have modeled the bulk composition of the Earth as an equilibrated assemblage along the basalt-harzburgite join because of the models proximity to mantle dynamical processes, i.e., melting of mantle material along mid-ocean ridges produces a basaltic crust, while leaving behind the harzburgitic component. This process produces a physically and chemically stratified lithosphere which is continuously

subducted into the deeper parts of the Earth providing a mechanism for the production of large-scale mantle heterogeneities. In spite of its simplicity, the concept of distinct chemical end-member compositions is found to provide an adequate description of mantle chemistry, at least from a geophysical point of view.

[70] We have used this model to invert a set of fundamental and higher-order Rayleigh (up to sixth overtone) and Love wave (up to fifth overtone) phase velocity dispersion curves for mantle composition and temperature at a number of locations covering four different geological settings. The data have sensitivity well below the TZ and thus provide a robust measure of the isotropic as well as anisotropic S wave velocity structure, in addition to isotropic P wave and density structure of the particular locations considered, reflecting lateral long-wavelength variations in mantle composition and temperature.

[71] Specifically, we found a radial gradient in basalt fraction that typically indicated basalt depletion in the upper mantle, in accordance with the melting scenario at mid-ocean ridges, and basalt enrichment in the lower mantle. However, gradients in basalt fraction were found to vary in size, mostly, while some locations also showed changes in sign, albeit small. With regard to mantle thermal structure, significant variations from adiabatic conditions were observed, which again depend on the particular location under consideration. The combined compositional/thermal variations showed up clearly in TZ structure, in particular, TZ thickness. Locales with “warmer” geotherms had a thinner TZ thickness relative to “colder” locales. This explains the lateral variations in location and size of the 410 and 660 that are observed in various seismological studies. Regarding anisotropy, the picture that emerges here is in overall accordance with previous analyses that reported $\xi > 0$ in the upper 200 km of the mantle, as well as strong regional variations in the anisotropic signal. Concerning the TZ and deeper mantle, we find little evidence for anisotropy in these regions, in agreement with a recent global 3-D anisotropic model.

[72] The lack of any strong compositional discontinuities, and associated thermal boundary layers, found here, is evidence in support of whole mantle over layered mantle convection. The former scenario is also strongly favored by the seismological evidence for penetration of slabs, which at the same time provides a natural mechanism for the introduction of heterogeneities, into the lower mantle. On the other hand, if whole mantle convection is the sole mode of operation, it is difficult to envisage how long-wavelength chemical and thermal variations in the mantle would survive. This likely points to a more complicated picture, where mantle dynamics is governed by a mixture of layered and whole mantle convection as discussed recently by Tackley [2008].

[73] Finally, and although the approach put forward here is able to reveal a more subtle picture of the mantle than are more traditional methods employed in the field of seismic tomography, application of the method for the determination of global 3-D mantle chemical and thermal structure is nonetheless limited given the computational resources currently available. At present a low-resolution ($20\text{--}30^\circ \times 20\text{--}30^\circ$) 3-D model is envisaged, as our future goal.

[74] **Acknowledgments.** We would like to extend our gratitude to a number of people who have contributed in various ways to this project by either providing data, K. Visser and J. Trampert; models, T. Nakagawa, P. Tackley and F. Cammarano; comments and suggestions early on, G. Ekström, S. Lebedev, G. Laske, and V. Maupin. We are also grateful to two anonymous reviewers for their comments that helped improve the manuscript. Finally, L. Boschi also wishes to thank D. Giardini for constant support and encouragement, while A. Khan acknowledges the support provided through funding from the Danish agency for Science, Technology and Innovation.

References

- Anderson, D. L. (1961), Elastic wave propagation in layered anisotropic media, *J. Geophys. Res.*, *66*, 2953, doi:10.1029/JZ066i009p02953.
- Anderson, D. L., and A. M. Dziewonski (1982), Upper mantle anisotropy: Evidence from free oscillations, *Geophys. J. R. Astron. Soc.*, *69*, 383.
- Anderson, D. L., and J. W. Given (1982), Absorption band Q model of the Earth, *J. Geophys. Res.*, *87*, 3893, doi:10.1029/JB087iB05p03893.
- Antolik, M., Ekstrom, and A. M. Dziewonski (2001), Global event location with full and sparse datasets using three-dimensional models of mantle P -wave velocity, *Pure Appl. Geophys.*, *158*, 291, doi:10.1007/PL00001161.
- Babuska, V., and M. Cara (1991), *Seismic Anisotropy in the Earth*, Kluwer Acad., Boston, Mass.
- Becker, T., and L. Boschi (2002), A comparison of tomographic and geodynamic mantle models, *Geochem. Geophys. Geosyst.*, *3*(1), 1003, doi:10.1029/2001GC000168.
- Beghein, C., and J. Trampert (2004), Probability density function for radial anisotropy from fundamental mode surface wave data and the neighbourhood algorithm, *Geophys. J. Int.*, *157*, 1163, doi:10.1111/j.1365-246X.2004.02235.x.
- Beghein, C., J. Trampert, and H. J. Van Heijst (2006), Radial anisotropy in seismic reference model of the mantle, *J. Geophys. Res.*, *111*, B02303, doi:10.1029/2005JB003728.
- Beucler, É., and J.-P. Montagner (2006), Computation of Large Anisotropic Seismic Heterogeneities (CLASH), *Geophys. J. Int.*, *165*, 447, doi:10.1111/j.1365-246X.2005.02813.x.
- Bijwaard, H., W. Spakman, and E. R. Engdahl (1998), Closing the gap between regional and global travel time tomography, *J. Geophys. Res.*, *103*, 30,055, doi:10.1029/98JB02467.
- Boschi, M. (1999), Lithologic tomography: From plural geophysical data to lithology estimation, *J. Geophys. Res.*, *104*, 749, doi:10.1029/1998JB900014.
- Boschi, L., and A. M. Dziewonski (1999), High and low resolution images of the Earth's mantle: Implications of different approaches to tomographic modeling, *J. Geophys. Res.*, *104*, 25,567, doi:10.1029/1999JB900166.
- Boschi, L., and A. M. Dziewonski (2000), Whole Earth tomography from delay times of P, PcP, PKP phases: Lateral heterogeneities in the outer core, or radial anisotropy in the mantle?, *J. Geophys. Res.*, *105*, 13,675, doi:10.1029/2000JB900059.
- Boschi, L., and G. Ekström (2002), New images of the Earth's upper mantle from measurements of surface wave phase velocity anomalies, *J. Geophys. Res.*, *107*(B4), 2059, doi:10.1029/2000JB000059.
- Boschi, L., T. W. Becker, and B. Steinberger (2008), On the statistical significance of correlations between synthetic mantle plumes and tomographic models, *Phys. Earth Planet. Inter.*, *167*, 230, doi:10.1016/j.pepi.2008.03.009.
- Brown, J. M., and T. J. Shankland (1981), Thermodynamic parameters in the Earth as determined from seismic profiles, *Geophys. J. R. Astron. Soc.*, *66*, 579.
- Cammarano, F., and B. Romanowicz (2007), Insights into the nature of the transition zone from physically constrained inversion of long period seismic data, *Proc. Natl. Acad. Sci. U.S.A.*, *104*, 9139, doi:10.1073/pnas.0608075104.
- Cammarano, F., B. Romanowicz, L. Stixrude, C. Lithgow-Bertelloni, and W. Xu (2009), Inferring the thermochemical structure of the upper mantle from seismic data, *Geophys. J. Int.*, in press.
- Carannante, S., and L. Boschi (2005), Databases of surface wave dispersion, *Ann. Geophys.*, *48*, 945.
- Christensen, U. R., and A. W. Hofmann (1994), Segregation of subducted oceanic crust in the convecting mantle, *J. Geophys. Res.*, *99*, 19,867, doi:10.1029/93JB03403.
- Connolly, J. A. D. (2005), Computation of phase equilibria by linear programming: A tool for geodynamic modeling and an application to subduction zone decarbonation, *Earth Planet. Sci. Lett.*, *236*, 524, doi:10.1016/j.epsl.2005.04.033.
- Connolly, J. A. D., and D. M. Kerrick (2002), Metamorphic controls on seismic velocity of subducted oceanic crust at 100–250 km depth, *Earth Planet. Sci. Lett.*, *204*, 61, doi:10.1016/S0012-821X(02)00957-3.

- Davies, G. (2006), Gravitational depletion of the earthy Earth's upper mantle and the viability of early plate tectonics, *Earth Planet. Sci. Lett.*, *243*, 376, doi:10.1016/j.epsl.2006.01.053.
- Debayle, E., and B. L. N. Kennett (2000), Anisotropy in the Australian upper mantle from Love and Rayleigh waveform inversion, *Earth Planet. Sci. Lett.*, *184*, 339, doi:10.1016/S0012-821X(00)00314-9.
- Debayle, E., B. L. N. Kennett, and K. Priestley (2005), Global azimuthal seismic anisotropy and the unique plate-motion deformation of Australia, *Nature*, *433*, 509, doi:10.1038/nature03247.
- Deschamps, F., and J. Trampert (2004), Towards a lower mantle reference temperature and composition, *Earth Planet. Sci. Lett.*, *222*, 161, doi:10.1016/j.epsl.2004.02.024.
- Deuss, A., and J. Woodhouse (2001), Seismic observations of splitting of the mid-transition zone discontinuity in Earth's mantle, *Science*, *294*, 354, doi:10.1126/science.1063524.
- Duffy, T., et al. (1995), Elasticity of forsterite to 16 GPa and the composition of the upper mantle, *Nature*, *378*, 170, doi:10.1038/378170a0.
- Dziewonski, A. M., and D. L. Anderson (1981), Preliminary reference Earth model, *Phys. Earth Planet. Inter.*, *25*, 297, doi:10.1016/0031-9201(81)90046-7.
- Ekström, G., and A. M. Dziewonski (1998), The unique anisotropy of the Pacific upper mantle, *Nature*, *394*, 168, doi:10.1038/28148.
- Flanagan, M. P., and P. M. Shearer (1999), A map of topography on the 410-km discontinuity from PP precursors, *Geophys. Res. Lett.*, *26*, 549, doi:10.1029/1999GL900036.
- Forsyth, D. W. (1975), The early structural evolution and anisotropy of the oceanic upper mantle, *Geophys. J. R. Astron. Soc. London*, *43*, 103.
- Grand, S. P. (1994), Mantle shear structure beneath the Americas and surrounding oceans, *J. Geophys. Res.*, *99*, 11,591, doi:10.1029/94JB00042.
- Grand, S. P., R. D. Van der Hilst, and S. Widiyantoro (1997), Global seismic tomography: A snapshot of convection in the Earth, *GSA Today*, *7*, 1.
- Gu, Y. J., and A. M. Dziewonski (2002), Global variability of transition zone thickness, *J. Geophys. Res.*, *107*(B7), 2135, doi:10.1029/2001JB000489.
- Gung, Y., M. Panning, and B. Romanowicz (2003), Global anisotropy and the thickness of continents, *Nature*, *422*, 707, doi:10.1038/nature01559.
- Helfrich, G. R. (2002), Chemical and seismological constraints on mantle heterogeneity, *Philos. Trans. R. Soc. London, Ser. A*, *360*, 2493, doi:10.1098/rsta.2002.1085.
- Helfrich, G. R. (2006), Heterogeneity in the mantle—Its creation, evolution and destruction, *Tectonophysics*, *416*, 23, doi:10.1016/j.tecto.2005.11.012.
- Helfrich, G. R., and B. J. Wood (2001), The Earth's mantle, *Nature*, *412*, 501, doi:10.1038/35087500.
- Hofmann, A. W. (1997), Mantle geochemistry: The message from oceanic volcanism, *Nature*, *385*, 219, doi:10.1038/385219a0.
- Ishii, M., and J. Tromp (1999), Normal-mode and free-air gravity constraints on lateral variations in velocity and density of Earth's mantle, *Science*, *285*, 1231, doi:10.1126/science.285.5431.1231.
- Ito, E., and E. Takahashi (1989), Postspinel transformations in the system Mg₂SiO₄-Fe₂SiO₄ and some geophysical implications, *J. Geophys. Res.*, *94*, 10,637, doi:10.1029/JB094iB08p10637.
- Jackson, I., J. D. Fitz Gerald, U. H. Faul, and B. H. Tan (2002), Grain-size-sensitive seismic wave attenuation in polycrystalline olivine, *J. Geophys. Res.*, *107*(B12), 2360, doi:10.1029/2001JB001225.
- Jung, H., and S. I. Karato (2001), Water-induced fabric transitions in olivine, *Science*, *293*, 1460, doi:10.1126/science.1062235.
- Karato, S.-I. (1993), Importance of anelasticity in the interpretation of seismic tomography, *Geophys. Res. Lett.*, *20*, 1623, doi:10.1029/93GL01767.
- Karato, S.-I. (1998), Seismic anisotropy in the deep mantle, boundary layers and the geometry of mantle convection, *Pure Appl. Geophys.*, *151*, 565, doi:10.1007/s000240050130.
- Kennett, B. L. N., E. R. Engdahl, and R. Buland (1995), Constraints on seismic velocities in the Earth from travel times, *Geophys. J. Int.*, *122*, 108, doi:10.1111/j.1365-246X.1995.tb03540.x.
- Khan, A., J. A. D. Connolly, and N. Olsen (2006), Constraining the composition and thermal state of the mantle beneath Europe from inversion of long-period electromagnetic sounding data, *J. Geophys. Res.*, *111*, B10102, doi:10.1029/2006JB004270.
- Khan, A., J. A. D. Connolly, J. Maclennan, and K. Mosegaard (2007), Joint inversion of seismic and gravity data for lunar composition and thermal state, *Geophys. J. Int.*, *168*, 243, doi:10.1111/j.1365-246X.2006.03200.x.
- Khan, A., J. A. D. Connolly, and S. R. Taylor (2008), Inversion of seismic and geodetic data for the major element chemistry and temperature of the Earth's mantle, *J. Geophys. Res.*, *113*, B09308, doi:10.1029/2007JB005239.
- Kustowski, B., G. Ekström, and A. M. Dziewonski (2008), Anisotropic shear wave velocity structure of the Earth's mantle: A global model, *J. Geophys. Res.*, *113*, B06306, doi:10.1029/2007JB005169.
- Lawrence, J. F., and P. M. Shearer (2006), Constraining seismic velocity and density for the mantle transition zone with reflected and transmitted waveforms, *Geochem. Geophys. Geosyst.*, *7*, Q10012, doi:10.1029/2006GC001339.
- Lebedev, S., T. Meier, and R. D. Van der Hilst (2006), Asthenospheric flow and origin of volcanism in the Baikal Rift area, *Earth Planet. Sci. Lett.*, *249*, 415, doi:10.1016/j.epsl.2006.07.007.
- Leveque, J. J., E. Debayle, and V. Maupin (1998), Anisotropy in the Indian Ocean upper mantle from Rayleigh- and Love-waveform inversion, *Geophys. J. Int.*, *133*, 529, doi:10.1046/j.1365-246X.1998.00504.x.
- Love, A. E. H. (1927), *A Treatise on the Theory of Elasticity*, Cambridge Univ. Press, Cambridge, U. K.
- Lyubetskaya, T., and J. Korenaga (2007), Chemical composition of Earth's primitive mantle and its variance: 1. Method and results, *J. Geophys. Res.*, *112*, B03211, doi:10.1029/2005JB004223.
- Maggi, H., E. Debayle, K. Priestley, and K. Barroul (2006), Multimode surface waveform tomography of the Pacific Ocean: A closer look at the lithospheric cooling signature, *Geophys. J. Int.*, *166*, 1384, doi:10.1111/j.1365-246X.2006.03037.x.
- Marone, F., Y. Gung, and B. Romanowicz (2007), Three-dimensional radial anisotropic structure of the North American upper mantle from the inversion of surface waveform data, *Geophys. J. Int.*, *171*, 206, doi:10.1111/j.1365-246X.2007.03465.x.
- Masters, G., G. Laske, H. Bolton, and A. M. Dziewonski (2000), The relative behaviour of shear velocity, bulk sound speed, and compressional velocity in the mantle: Implications for chemical and thermal structure, in *Earth's Deep Interior: Mineral Physics and Tomography From the Atlantic to the Global Scale*, *Geophys. Monogr. Ser.*, vol. 117, edited by S. Karato et al., p. 63, AGU, Washington, D. C.
- Maupin, V., and M. Cara (1992), Love-Rayleigh wave incompatibility and possible deep upper mantle anisotropy in the Iberian Peninsula, *Pure Appl. Geophys.*, *138*, 429, doi:10.1007/BF00876881.
- McEvelly, T. V. (1964), Central US crust-upper mantle structure from Love and Rayleigh wave phase velocity inversion, *Bull. Seismol. Soc. Am.*, *54*, 1977.
- Montagner, J. P. (1998), Where can seismic anisotropy be detected in the Earth's mantle?, *Pure Appl. Geophys.*, *151*, 223, doi:10.1007/s000240050113.
- Montagner, J. P., and B. L. N. Kennett (1996), How to reconcile body-wave and normal-mode reference Earth models, *Geophys. J. Int.*, *125*, 229, doi:10.1111/j.1365-246X.1996.tb06548.x.
- Nakagawa, T., P. J. Tackley, F. Deschamps, and J. A. D. Connolly (2009), Incorporating self-consistently calculated mineral physics into thermochemical mantle convection simulations in a 3-D spherical shell and its influence on seismic anomalies in Earth's mantle, *Geochem. Geophys. Geosyst.*, *10*, Q03004, doi:10.1029/2008GC002280.
- Nataf, H. C., I. Nakanishi, and D. L. Anderson (1986), Measurements of mantle velocities and inversion for lateral heterogeneities and anisotropy: 3. Inversion, *J. Geophys. Res.*, *91*, 7261, doi:10.1029/JB091iB07p07261.
- Nettles, M., and A. M. Dziewonski (2008), Radially anisotropic shear-velocity structure of the upper mantle globally and beneath North America, *J. Geophys. Res.*, *113*, B02303, doi:10.1029/2006JB004819.
- Nishimura, C. E., and D. W. Forsyth (1989), The anisotropic structure of the upper mantle in the Pacific, *Geophys. J.*, *96*, 203, doi:10.1111/j.1365-246X.1989.tb04446.x.
- Panning, M., and B. Romanowicz (2004), Inferences on flow at the base of Earth's mantle based on seismic anisotropy, *Science*, *303*, 351, doi:10.1126/science.1091524.
- Panning, M., and B. Romanowicz (2006), A three-dimensional radially anisotropic model of shear velocity in the whole mantle, *Geophys. J. Int.*, *167*, 361, doi:10.1111/j.1365-246X.2006.03100.x.
- Qin, Y., Y. Capdeville, J.-P. Montagner, L. Boschi, and T. W. Becker (2009), Reliability of mantle tomography models assessed by spectral-element simulations, *Geophys. J. Int.*, *177*, 125, doi:10.1111/j.1365-246X.2008.04032.x.
- Ringwood, A. E. (1975), *Composition and Petrology of the Earth's Mantle*, McGraw-Hill, New York.
- Ritsema, J., H. J. van Heijst, and J. H. Woodhouse (2004), Global transition zone tomography, *J. Geophys. Res.*, *109*, B02302, doi:10.1029/2003JB002610.
- Ritsema, J., W. Xu, L. Stixrude, and C. Lithgow-Bertelloni (2009), Estimates of the transition zone temperature in a mechanically mixed upper mantle, *Earth Planet. Sci. Lett.*, *244*, doi:10.1016/j.epsl.2008.10.024.
- Romanowicz, B., and B. Mitchell (2007), Deep Earth structure—Q of the Earth from crust to core, in *Treatise on Geophysics*, vol. 1, *Seismology and Structure of the Earth*, edited by G. Schubert, p. 731, Elsevier, New York.

- Sambridge, M. (1999), Geophysical inversion with a neighbourhood algorithm—I. Searching a parameter space, *Geophys. J. Int.*, *138*, 479, doi:10.1046/j.1365-246X.1999.00876.x.
- Sebai, A., E. Stutzmann, and J. P. Montagner (2006), Anisotropic structure of the African upper mantle structure from Rayleigh and Love wave tomography, *Phys. Earth Planet. Inter.*, *155*, 48, doi:10.1016/j.pepi.2005.09.009.
- Shapiro, N. M., and M. H. Ritzwoller (2002), Monte-Carlo inversion for a global shear-velocity model of the crust and upper mantle, *Geophys. J. Int.*, *151*, 88, doi:10.1046/j.1365-246X.2002.01742.x.
- Shapiro, N. M., and M. H. Ritzwoller (2004), Thermodynamic constraints on seismic inversions, *Geophys. J. Int.*, *157*, 1175, doi:10.1111/j.1365-246X.2004.02254.x.
- Silveira, G., and E. Stutzmann (2002), Tomography of the Atlantic Ocean, *Phys. Earth Planet. Inter.*, *132*, 237, doi:10.1016/S0031-9201(02)00076-6.
- Stacey, F. D., and P. M. Davis (2004), High pressure equations of state with applications to the lower mantle and core, *Phys. Earth Planet. Inter.*, *142*, 137, doi:10.1016/j.pepi.2004.02.003.
- Steinberger, B., and A. Calderwood (2006), Models of large-scale viscous flow in the Earth's mantle with constraints from mineral physics and surface observations, *Geophys. J. Int.*, *167*, 1461, doi:10.1111/j.1365-246X.2006.03131.x.
- Stixrude, L., and R. Jeanloz (2007), Constraints on seismic models from other disciplines—Constraints from mineral physics on seismological models, in *Treatise on Geophysics*, vol. 1, *Seismology and Structure of the Earth*, edited by G. Schubert, p. 775, Elsevier, New York.
- Stixrude, L., and C. Lithgow-Bertelloni (2005), Mineralogy and elasticity of the oceanic upper mantle: Origin of the low-velocity zone, *J. Geophys. Res.*, *110*, B03204, doi:10.1029/2004JB002965.
- Stixrude, L., and C. Lithgow-Bertelloni (2007), Influence of phase transformations on lateral heterogeneity and dynamics in Earth's mantle, *Earth Planet. Sci. Lett.*, *263*, 45, doi:10.1016/j.epsl.2007.08.027.
- Tackley, P. J. (2008), Geodynamics: Layer cake or plum pudding?, *Nat. Geosci.*, *1*, 157, doi:10.1038/ngeo134.
- Tackley, P. J., S. Xie, T. Nakagawa, and J. W. Hernlund (2005), Numerical and laboratory studies of mantle convection: Philosophy, accomplishments and thermo-chemical structure evolution, in *Earth's Deep Mantle: Structure, Composition and Evolution*, *Geophys. Monogr. Ser.*, vol. 160, edited by R. D. Van Der Hilst et al., p. 83, AGU, Washington, D. C.
- Tanimoto, T., and D. L. Anderson (1984), Mapping convection in the mantle, *Geophys. Res. Lett.*, *11*, 287, doi:10.1029/GL011i004p00287.
- Tarantola, A., and B. Valette (1982), Inverse problems: Quest for information, *J. Geophys.*, *50*, 159.
- Trampert, J., F. Deschamps, J. Resovsky, and D. Yuen (2004), Chemical heterogeneities throughout the lower mantle, *Science*, *306*, 853, doi:10.1126/science.1101996.
- Van der Hilst, R., R. Engdahl, W. Spakaman, and G. Nolet (1991), Tomographic imaging of subducted lithosphere below northwest Pacific island arcs, *Nature*, *353*, 37, doi:10.1038/353037a0.
- Van der Hilst, R., S. Widyantoro, and E. R. Engdahl (1997), Evidence for deep mantle circulation from global tomography, *Nature*, *386*, 578, doi:10.1038/386578a0.
- Visser, K., J. Trampert, and B. L. N. Kennett (2008a), Global anisotropic phase-velocity maps for higher mode Love and Rayleigh waves, *Geophys. J. Int.*, *172*, 1016, doi:10.1111/j.1365-246X.2007.03685.x.
- Visser, K., J. Trampert, S. Lebedev, and B. L. N. Kennett (2008b), Probability of radial anisotropy in the deep mantle, *Earth Planet. Sci. Lett.*, *270*, 241, doi:10.1016/j.epsl.2008.03.041.
- Xie, S., and P. J. Tackley (2004), Evolution of helium and argon isotopes in a convecting mantle, *Phys. Earth Planet. Inter.*, *146*, 417, doi:10.1016/j.pepi.2004.04.003.
- Xu, W., C. Lithgow-Bertelloni, L. Stixrude, and J. Ritsema (2008), The effect of bulk composition and temperature on mantle seismic structure, *Earth Planet. Sci. Lett.*, *275*, 70, doi:10.1016/j.epsl.2008.08.012.
- Zhou, Y., G. Nolet, F. A. Dahlen, and G. Laske (2006), Global upper mantle structure from finite frequency surface wave tomography, *J. Geophys. Res.*, *111*, B04304, doi:10.1029/2005JB003677.

L. Boschi, Institute of Geophysics, Swiss Federal Institute of Technology, Supersaturates 5, CH-8092 Zurich, Switzerland. (larryboschi@gmail.com)

J. A. D. Connolly, Institute for Mineralogy and Petrology, Swiss Federal Institute of Technology, Clausiusstrasse 25, CH-8092 Zurich, Switzerland. (james.connolly@erdw.ethz.ch)

A. Khan, Niels Bohr Institute, University of Copenhagen, Juliane Maries Vej 30, DK-2100 Copenhagen Oe, Denmark. (amir@gfy.ku.dk)